UNCLASSIFIED

AD NUMBER
AD251122
LIMITATION CHANGES
TO: **Approved for public release; distribution is unlimited.**
FROM: **Distribution authorized to U.S. Gov't. agencies and their contractors; Administrative/Operational Use; NOV 1960. Other requests shall be referred to Air Force Cambridge Research Laboratory, Hanscom AFB, MA.**
AUTHORITY
AFCRL ltr dtd 3 Nov 1971

THIS PAGE IS UNCLASSIFIED

UNCLASSIFIED

AD 251 122

Reproduced
by the

ARMED SERVICES TECHNICAL INFORMATION AGENCY
ARLINGTON HALL STATION
ARLINGTON 12, VIRGINIA

UNCLASSIFIED

BEST
AVAILABLE COPY

NOTICE: When government or other drawings, specifications or other data are used for any purpose other than in connection with a definitely related government procurement operation, the U. S. Government thereby incurs no responsibility, nor any obligation whatsoever; and the fact that the Government may have formulated, furnished, or in any way supplied the said drawings, specifications, or other data is not to be regarded by implication or otherwise as in any manner licensing the holder or any other person or corporation, or conveying any rights or permission to manufacture, use or sell any patented invention that may in any way be related thereto.

AFCRL-TN-60-835

Contract AF 19(604)-5961

ASTIA 251 122

Scientific Report 2

DISTRIBUTIONS OF ATMOSPHERIC RADIATIVE HEATING AND COOLING

829 800

By: *K. L. Coulson* *P. M. Furukawa*

SRI Project No. 2994

FEB 23 1961

Prepared for:

GEOPHYSICS RESEARCH DIRECTORATE
AIR RESEARCH AND DEVELOPMENT COMMAND

AIR FORCE RESEARCH DIVISION
BEDFORD, MASSACHUSETTS

THROUGH SUPPORT OF THE ADVANCED RESEARCH PROJECTS AGENCY

STANFORD RESEARCH INSTITUTE

MENLO PARK, CALIFORNIA

*SRI

61-2-2
XEROX

STANFORD RESEARCH INSTITUTE
MENLO PARK, CALIFORNIA

November 1960

Scientific Report 2

DISTRIBUTIONS OF ATMOSPHERIC RADIATIVE HEATING AND COOLING

Prepared for:

GEOPHYSICS RESEARCH DIRECTORATE
AIR RESEARCH AND DEVELOPMENT COMMAND

AIR FORCE RESEARCH DIVISION
BEDFORD, MASSACHUSETTS

THROUGH SUPPORT OF THE ADVANCED RESEARCH PROJECTS AGENCY

Contract AF 19(604)-5965
ARPA Order No. 26-59

By: K. L. Coulson P. M. Furukawa

SRI Project No. 2994

Approved:

for C R Gleason
E. A. POST, MANAGER RADIO AND WEATHER SCIENCES LABORATORY

D K Scheuch
D. R. SCHEUCH, ASSISTANT DIRECTOR OF ENGINEERING RESEARCH

Copy No. 23

ABSTRACT

The time variation of the atmospheric radiation regime is investigated for a selected synoptic situation. Elsasser's graphical method shows the diurnal variation of the upward-directed long-wave flux to be in phase with surface temperature changes, but no such change of downward flux was found. Clouds reduce the upward flux above the cloud tops and increase the downward flux below their bases. Long-wave radiative cooling is greatest above cloud tops and at upper surfaces of inversions. Ground surface temperature is shown to be very important in the long-wave regime.

Short-wave molecular scattering and surface reflection are evaluated for a model atmosphere by Chandrasekhar's exact method and are adapted for the synoptic situation. Water vapor absorption, ozone absorption, and the effects of atmospheric dust are approximated. Surface reflection, water vapor absorption, and absorption by particulates in a polluted atmosphere all play dominant roles, while the effects of molecular scattering and ozone absorption are relatively minor in the over-all energy regime.

CONTENTS

ABSTRACT ii

LIST OF ILLUSTRATIONS v

LIST OF TABLES vii

I INTRODUCTION 1

II THE SYNOPTIC SITUATION 3

III MODELING OF THE SYNOPTIC SITUATION 6

IV THE LONG-WAVE TERRESTRIAL RADIATION REGIME 9

A. General 9

B. Method of Computation 9

C. Upward Flux 10

D. Upward Flux at the Tropopause 13

E. Downward Flux 14

F. Downward Flux at the Ground 16

G. Flux Divergence 17

H. Loss of Energy by the Troposphere 20

I. Effects of Ground Surface Temperature 21

J. Summary 23

V THE SHORT-WAVE SOLAR RADIATION REGIME 25

A. General 25

B. Molecular Scattering and Surface Reflections 25

1. Introduction 25
2. Method of Calculation 26
3. Effect of Surface Reflectivity 27
4. Effect of Solar Angle 28
5. Variation with Altitude of Reflecting Surface . . 34
6. Discussion 38
7. Application to Synoptic Situation 40

CONTENTS (Concluded)

C. Absorption by Water Vapor 40

1. Absorption for Clear-Sky Conditions 42
2. Absorption for Overcast Conditions 43

D. Effects of Haze and Dust 47

E. Ozone Absorption of Solar Radiation 58

ACKNOWLEDGMENT 63

APPENDIX--THE MONOCHROMATIC REFLECTANCE R_ν OF THE ATMOSPHERE-SURFACE SYSTEM FOR VARIOUS VALUES OF THE OPTICAL THICKNESS τ AND SURFACE REFLECTIVITY, A 64

REFERENCES 68

ILLUSTRATIONS

Fig. 1 Synoptic Situation over U.S., 1830Z, 14 March 1957 . . . 4

Fig. 2 Schematic Representation of the Synoptic Situation at Omaha During 12-16 March 1957 7

Fig. 3 Distribution of the Upward Long-Wave Radiative Flux at Omaha During 12-16 March 1957 11

Fig. 4 Distribution of the Downward Long-Wave Radiative Flux at Omaha During 12-16 March 1957 15

Fig. 5 Distribution of Long-Wave Flux Divergence (Rate of Cooling) at Omaha During 12-16 March 1957 18

Fig. 6 The Effect of the Ground Surface Temperature on the Upward and Net Long-Wave Flux Distributions 22

Fig. 7 Monochromatic Reflectance of Model Atmosphere-Plus-Surface System as a Function of Surface Reflectivity for Optical Thickness $\tau = 1.00$ for Five Different Solar Zenith Angles 29

Fig. 8 Monochromatic Reflectance of Model Atmosphere-Plus-Surface System as a Function of Surface Reflectivity for Optical Thickness $\tau = 0.10$ for Five Different Solar Zenith Angles 30

Fig. 9 Monochromatic Reflectance of Model Atmosphere-Plus-Surface System as a Function of Surface Reflectivity for Optical Thickness $\tau = 0.001$ for Five Different Solar Zenith Angles 31

Fig. 10 Reflectance of Model Atmosphere-Plus-Surface System as a Function of Cosine of Solar Zenith Angle μ_o for Spectral Interval 3100 Å $\leq \lambda \leq$ 25,000 Å for Different Values of Surface Reflectivity 32

Fig. 11 Reflectance of Model Atmosphere-Plus-Surface System as a Function of Cosine of Solar Zenith Angle μ_o with Spectrum Divided into Ultraviolet (3100 Å $< \lambda <$ 4000 Å), Visible (4000 Å $< \lambda <$ 7000 Å), and Infrared (7000 Å $< \lambda <$ 25,000 Å) 33

Fig. 12 Upward Flux from the Top of Model Atmosphere as a Function of Wavelength for Solar Zenith Angle 66.4° with a Surface of Reflectivity 0.50 Located at Different Altitudes 35

ILLUSTRATIONS (Continued)

Fig. 13 Upward Flux from the Top of Model Atmosphere as a Function of Wavelength for Solar Zenith Angle 88.9° with a Surface of Reflectivity 0.50 Located at Different Altitudes 36

Fig. 14 System Reflectance as a Function of Altitude of Surface of Reflectivity 0.50, for the Ultraviolet (3100 Å < λ < 4000 Å) at Four Different Solar Zenith Angles 37

Fig. 15 System Reflectance as a Function of Altitude of Surface of Reflectivity 0.50 for Visible (4000 Å < λ < 7000 Å) and Infrared (7000 Å < λ < 25,000 Å) at Four Different Solar Zenith Angles 38

Fig. 16 Upward Flux of Solar Radiation from the Top of the Atmosphere and Solar Energy Absorbed by Ground at Omaha as a Function of Local Time for a Selected Synoptic Situation in March 1957 41

Fig. 17 Rate of Solar Energy Absorption by Atmospheric Water Vapor at Omaha as a Function of Local Time for Selected Synoptic Situation 45

Fig. 18 Schematic Diagram of Three-Layer Atmospheric Model . . 51

Fig. 19 Fractional Distribution of Extraterrestrial Incident Energy at Omaha as a Function of Local Time, for Clear and Industrially Polluted Atmospheric Conditions 54

Fig. 20 Distribution of Incident Solar Energy at Omaha as a Function of Local Time, for Clear and Industrially Polluted Atmospheric Conditions 55

Fig. 21 Fraction of Incident Energy Backscattered to Space by Clear Atmosphere 57

Fig. 22 Measured Vertical Distributions of Ozone (Solid Curves) at Arosa and White Sands, and Exponential Extrapolation (Dashed Curve) Assumed for Omaha 59

Fig. 23 Rate of Heating by Ozone Absorption of Solar Radiation as a Function of Height for Different Solar Zenith Angles 60

Fig. 24 Diurnal Temperature Increase by Ozone Absorption of Solar Radiation at Omaha in March 1957, as a Function of Height 61

Fig. 25 Rate of Solar Energy Absorption by Ozone at Omaha in March 1957, as a Function of Local Time 62

TABLES

Table I Total Solar Energy and Percent of Extraterrestrial Incident Flux Absorbed by Atmospheric Water Vapor at Omaha During Each Day of the Period, 12-15 March 1957 46

Table II Solar Energy Distribution by Atmospheric Processes for the Entire Day for Different Atmospheric Conditions at Omaha 56

Table III Fractions of Extraterrestrial Vertical Solar Energy Flux Absorbed and Backscattered by Atmospheric Particulates at Kew (After Blackwell, et al.) 57

DISTRIBUTIONS OF ATMOSPHERIC RADIATIVE HEATING AND COOLING

I INTRODUCTION

The present study is an evaluation of the long-wave and short-wave radiative energy transfers in a synoptic situation selected as being typical. The motivation for the study was two-fold. First is the need for non-adiabatic heating functions for use in dynamical-numerical atmospheric models. Secondly, the imminent availability of satellite radiation measurements makes it highly desirable to study the relation between the energy fluxes emerging from the top of the atmosphere and the processes occurring within the atmosphere.

The report covers a case study of the radiative energy transfers in a vertical column over a given station as a function of time during the passage of a weather system. The selection of a station for the study and the general synoptic conditions are described in Sec. II of the report. In order to facilitate the computations and the analyses of the flux distributions, the synoptic situation was idealized; the method and assumptions used to accomplish this are discussed in Sec. III.

The studies of the long-wave regime and the short-wave regime were conducted separately and are accordingly reported separately in Secs. IV and V. In the long-wave regime, only the radiative exchanges due to the absorption and emission by water vapor are considered. The fluxes are determined by means of Elsasser's radiation chart[3]* and their distributions are presented in a series of time cross sections. The study of the short-wave regime investigates the molecular scattering and surface

---

* All references are listed at the end of the report.

reflection of solar radiant energy by the use of the exact theory of radiative transfer as first derived by Chandrasekhar.[9] Water vapor absorption of short-wave radiation is examined by an empirical method developed by Korb, et al.,[11] and the effects of haze and dust are determined by means of a three-layered atmospheric model. The rate of heating by ultraviolet absorption of ozone is calculated on the basis of the latest information on ozone distribution.

Concurrent investigations under this project are concerned with the dynamical significance of non-adiabatic heating and cooling distributions on the evolution of atmospheric circulations. Dynamical-numerical integration with prescribed fields of heating rates are carried out for this purpose. This work will appear in a later report. These parallel investigations should lead to dependent heating formulations which will be useful in further realization of the inherent predictability of atmospheric motions and the weather.

II THE SYNOPTIC SITUATION

The selection of a station for the case study required that the station have (1) sufficient meteorological data to facilitate the computations of radiation fluxes, (2) a cyclone or frontal passage to bring about changes in the state of the atmosphere, (3) clear-sky conditions before and after the passage of the disturbance as "references," and (4) a location preferably on flat, continental terrain.

The station selected as meeting these requirements was Omaha, Nebraska, which experienced a cyclone-frontal passage during the period 12-16 March 1957. At the beginning of the period (12 March 1957) almost the entire Midwest, including Omaha, was under a weak high-pressure system and, except for a few scattered cirrus, clear skies prevailed throughout most of the area. On the 13th of March, a weak low situated on the lee-side of the Rocky Mountains initiated a regeneration with an accompanying frontogenesis. This continued to develop on the 14th, the center of the low and the polar front with its associated weather passing through Omaha at about 0300Z on this date. This was followed on the 15th and 16th by the outbreak of cold continental polar air behind the front and a build-up of a high-pressure cell with clear skies over Omaha and much of the Midwest. Figure 1 shows the synoptic situation over the United States at 1830Z, 14 March 1957.

The time-section analysis of the synoptic situation, as well as the flux computations and the analyses of the radiation fields, was based on the usual meteorological data (pressure, temperature, humidity) as published in the U.S. Weather Bureau's Northern Hemisphere Data Tabulation and on synoptic data (WBAN 10A and B) obtained from the National Weather Records Center. Lack of data on the moisture distribution above 400 mb made it necessary to extrapolate the moisture curve to the tropopause level in all cases. The procedure used here was to extend the dewpoint sounding upward from the point of its termination with a curve that

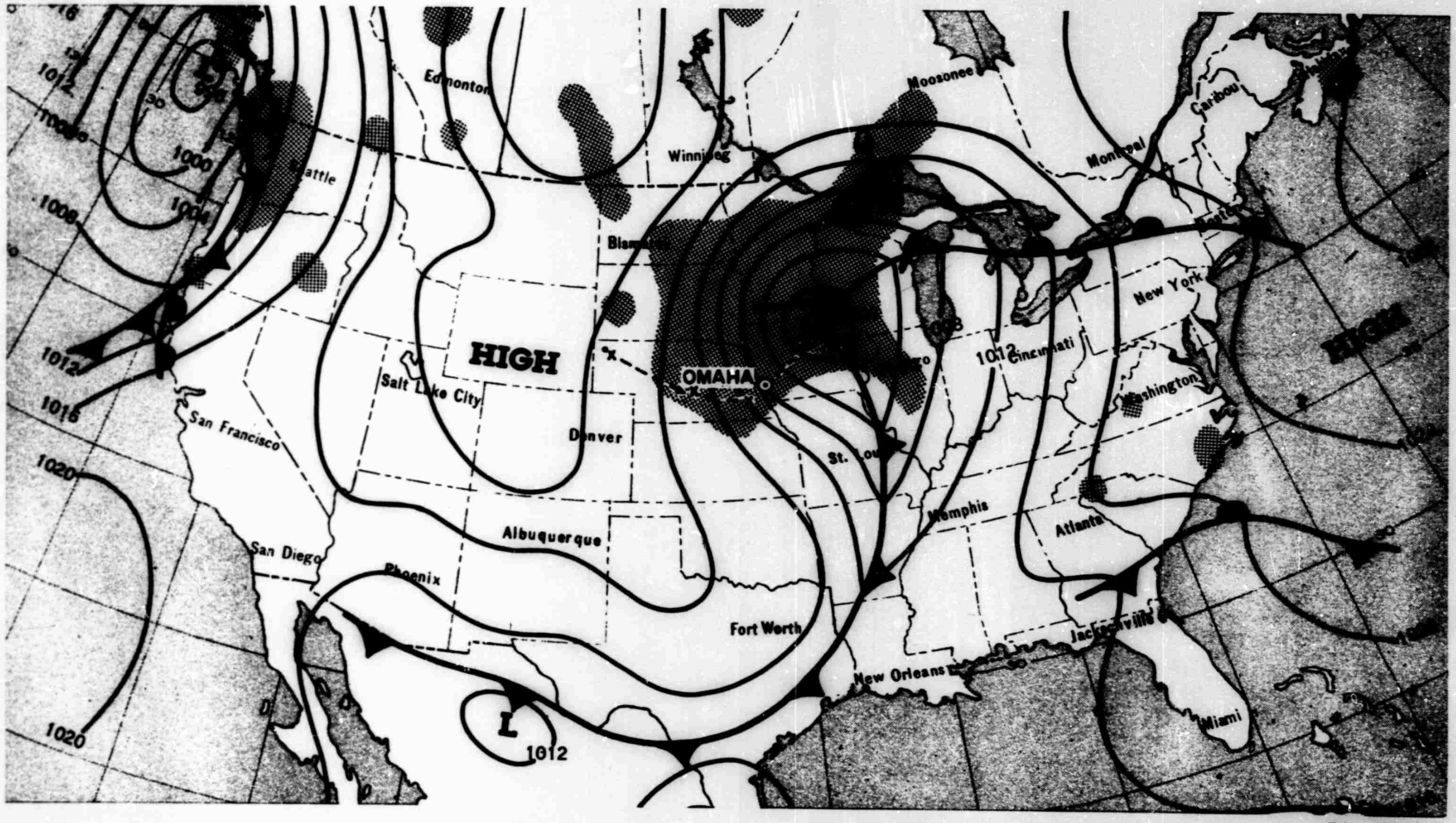

RA-2994-7

FIG. 1

SYNOPTIC SITUATION OVER U.S., 1830Z, 14 MARCH 1957
From USWB Daily Weather Map Series, U.S. Dept. of Commerce

paralleled the mean moisture distribution at the latitude for Omaha as given by London.[1]

Insufficient data on the heights of the cloud bases and tops also posed a serious obstacle in the determination of the radiation fluxes. Some information on cloud-base heights was available from the synoptic reports, but values of cloud-top heights were completely lacking. Estimates were made by using the synoptic reports and the cloud analysis criteria employed by Wilk[2] as guides and subjectively analyzing the meteorological soundings.

III MODELING OF THE SYNOPTIC SITUATION

The usual synoptic time cross-sectional analysis of the meteorological parameters (i.e., pressure, temperature, moisture plus clouds, frontal surface and weather) presented much too complex a picture of the changing atmospheric state for computing radiative fluxes. In order to make it more tractable for our study, the original time cross-sectional analysis was simplified by reproducing the synoptic situation in a schematic representation as shown in Fig. 2. In the model, the vertical distributions of pressure, temperature, and moisture as reported in the observational data were faithfully retained, for the most part, but the field of each parameter was smoothed of some detail. An observation of blowing dust reported during one period was omitted because it added complications requiring study that was beyond the scope of the present effort.

The most significant modification of the synoptic conditions was made with respect to the cloud distributions. Besides the previously mentioned lack of data on the heights of cloud tops, the complexity introduced into the radiation field by the physical parameters of the clouds compelled gross simplifications to be made as follows: (1) all clouds were assumed to be black bodies and only radiation from their tops and bases was considered, (2) all amounts of cloudiness were considered as moving over the station as one smooth-surfaced cloud body, (3) the period for the radiation field to go from the clear-sky condition to cloudy condition was assumed to be two hours for all amounts of cloudiness, (4) a discontinuity in the flux distribution was considered to occur right at the leading and trailing edges of the cloud layers, (5) heavy continuous precipitation was also assumed to be black body and was considered together with the accompanying cloud as such, and (6) multi-layered clouds were assumed continuous in the vertical such as to form a single layer. In the case of the partial cloudiness the fluxes were determined by weighting the fluxes according to the following formula:

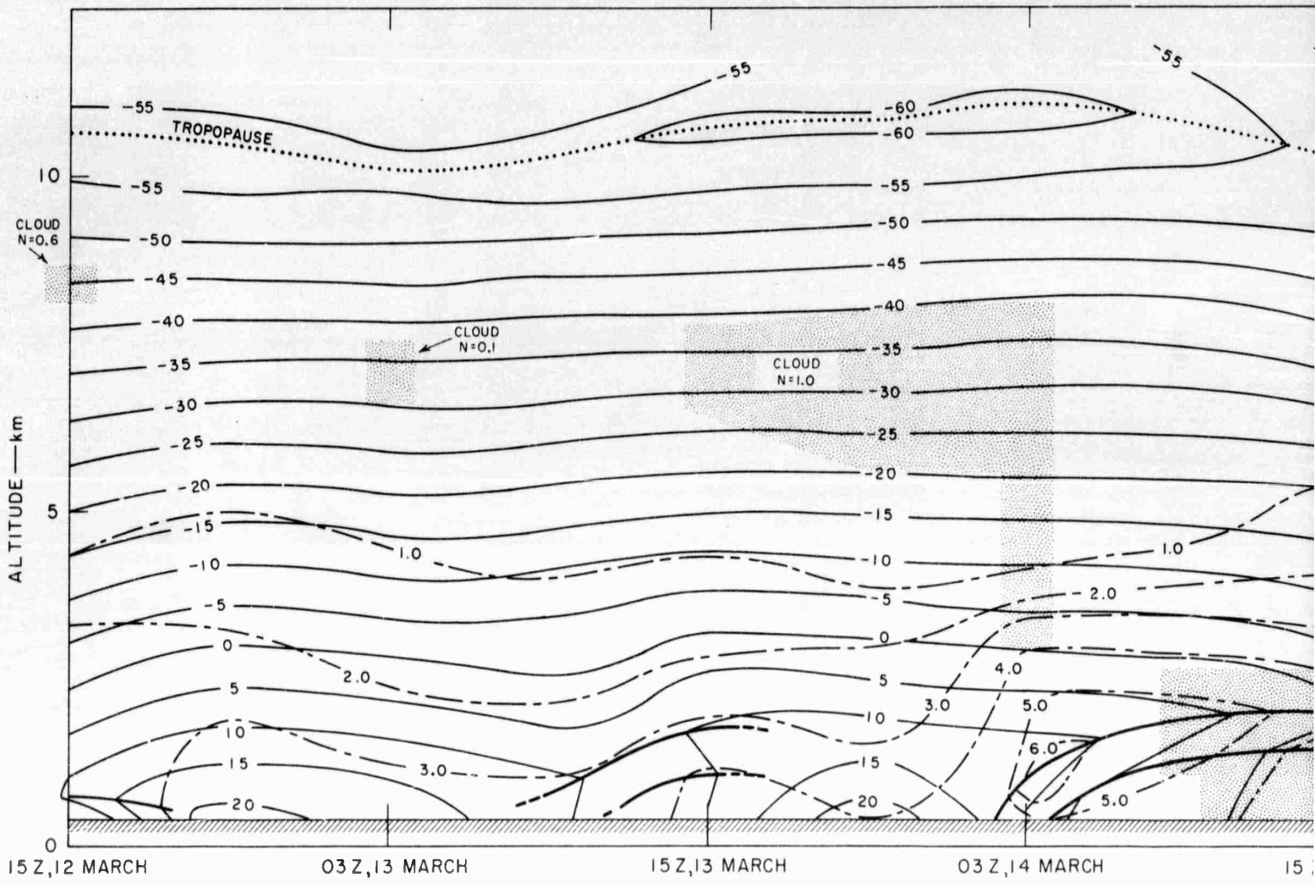

FIG. 2

SCHEMATIC REPRESENTATION OF THE SYNOPTIC SITUATION AT
Thin solid lines are isotherms in °C, dash-dot lines are is
in g/kg, front and inversions are represented by

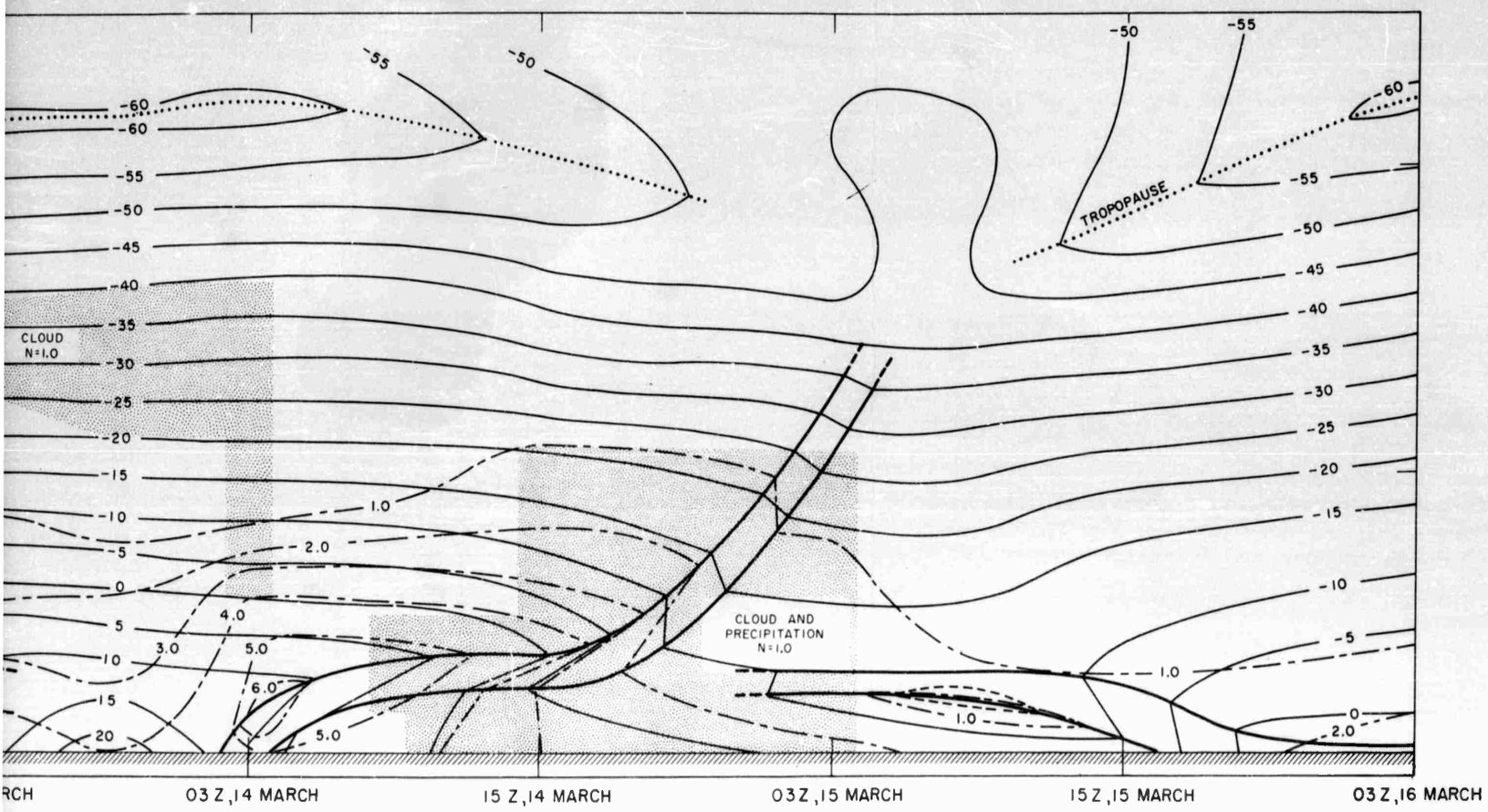

RD—2994—8

FIG. 2

REPRESENTATION OF THE SYNOPTIC SITUATION AT OMAHA DURING 12-16 MARCH 1957
id lines are isotherms in °C, dash-dot lines are isopleths of constant mixing ratio
in g/kg, front and inversions are represented by heavy solid lines.

2

$$F_P = F_C(1 - N) + F_O(N)$$

where F_P is the weighted flux value for partial cloud cover condition, F_C is the flux value for clear sky condition, F_O, is the flux value for overcast conditions, N is the amount of cloud cover in tenths of the sky. N = 1.0 indicates overcast conditions, and N = 0 indicates no cloud conditions.

There is no measurement on a regular routine basis of the soil surface temperature which is needed for determining the flux of radiant energy emitted by the earth's surface. Thus in the time section, the ground surface temperature was assumed to be equivalent to the reported surface air temperature of the meteorological observations. The effects and consequences of this assumption are discussed in a later section.

IV THE LONG-WAVE TERRESTRIAL RADIATION REGIME

A. GENERAL

The primary interests in the study of the long-wave terrestrial radiation were the determination of the long-wave flux distribution and its variations within the troposphere during changing synoptic conditions, the examination of the physical processes responsible for bringing about the variations, and the determination of the heating or cooling occurring in the troposphere resulting from long-wave radiative exchanges. Another aspect of the study was to relate the emergent radiant fluxes from the top of the atmosphere, as might be detected by a satellite, with the radiation processes within the atmosphere.

The atmospheric constituents that are important for the absorption of radiant energy within the spectral range of terrestrial radiation are water vapor, carbon dioxide, and ozone. Although at any level (especially the higher levels) of the troposphere, the carbon dioxide flux may be a significant percentage of either the total upward or downward long-wave flux; its net contribution to long-wave radiative temperature changes in the troposphere is generally very minor compared to that of water vapor. For our purposes, it was considered insignificant. Similarly the effects of tropospheric ozone were not included in the present study since the small concentration of this gas makes its role in the tropospheric radiative cooling or heating processes inappreciable. Thus, the present study of terrestrial radiation considered only the radiative exchanges due to the absorption and emission by water vapor which, in addition to its important absorptive properties, is distributed within the troposphere in greater amounts than the other two absorbing gases.

B. METHOD OF COMPUTATION

Elsasser's[3] graphical method was employed in the computations of the upward flux, F_u, and the downward flux, F_d, and from these two the net flux, F_n, and the flux divergence were determined. While it is understood

that later, improved methods of computing fluxes of long-wave radiation are available, the use of Elsasser's earlier technique is justified on the basis of (1) convenience, and (2) the fact that the values obtained are thought to be sufficiently accurate to give a valid pattern and the essential changes of the distribution of the radiation parameters.

The optical path length, which was used in computing the fluxes from the radiation charts, was corrected for the pressure-dependence of line-broadening in the water-vapor spectrum according to London[1]. In its final form, the corrected optical path length, u, is defined as:

$$u = \frac{0.5}{g} \int_{p_2}^{p_1} w \left(\frac{p_1}{p_s}\right) dp$$

where $\underline{g}$ is the acceleration due to gravity, $\underline{w}$ is the mixing ratio, p_1 and p_2 are the pressures at lower and upper boundaries, respectively, of the atmospheric layer, and p_s is the standard pressure, 1000 mb.

Flux computations were made to the tropopause (250-to-300-mb region) using the mandatory levels of the radiosonde reports as reference levels. Computations were made at additional levels at those times when an inversion, a frontal surface, or a cloud was present. Since the meteorological data were available only at 12-hour intervals, supplementary soundings were composed from the synoptic time section for 6-hour periods. Flux computations were then made for the shorter periods in order to aid in the analyses of the radiation flux fields.

C. UPWARD FLUX

Figure 3 represents the time-sectional analysis of the upward flux, F_u, of terrestrial radiation. It displays definite patterns of distribution which show that F_u generally decreases with height and that the largest decreases take place in the lower troposphere where the water-vapor concentration is the greatest.

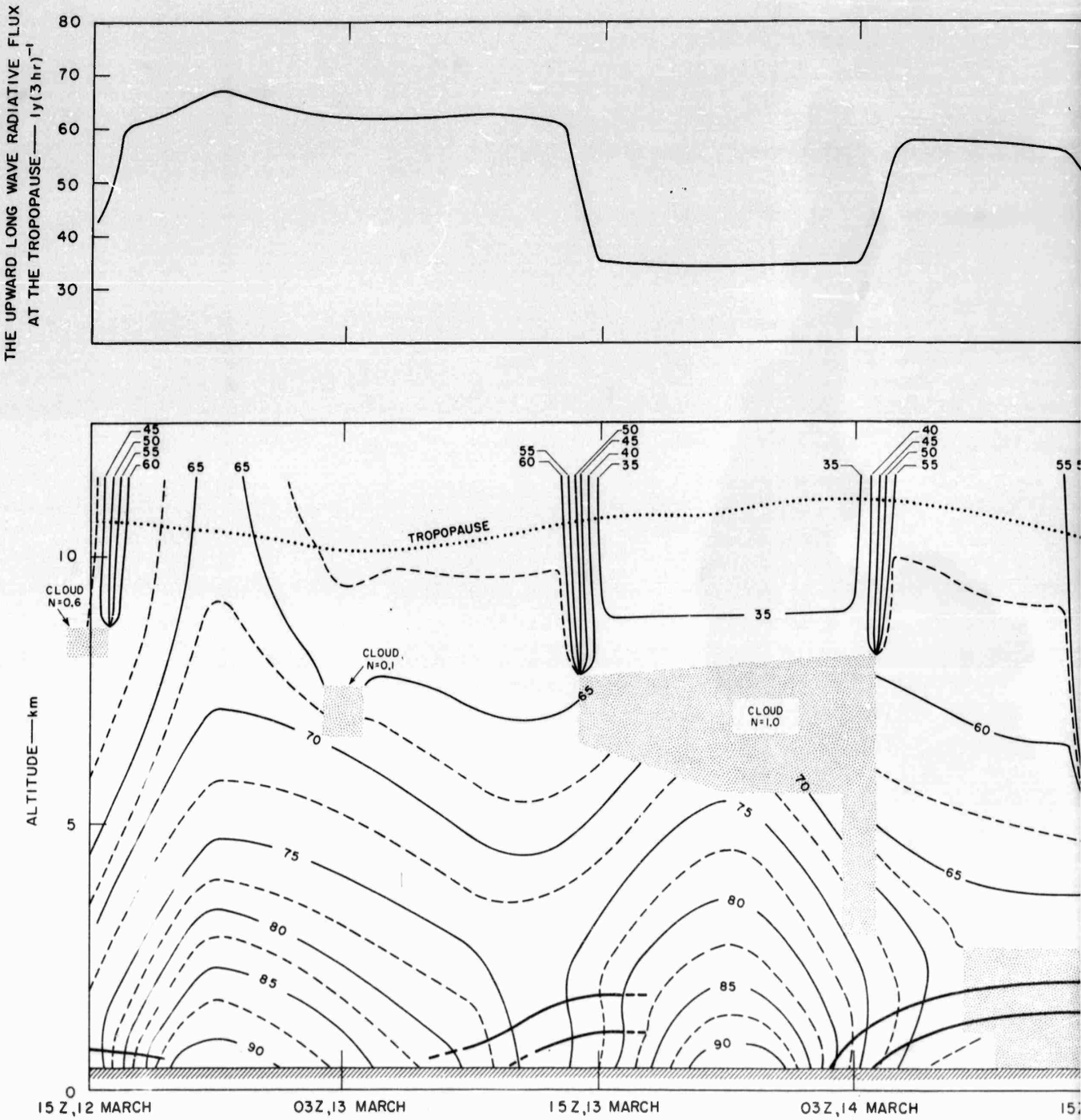

FIG. 3

DISTRIBUTION OF THE UPWARD LONG-WAVE RADIATIVE FLUX
Units: ly/3 hr. The dashed lines represent flux values in
given by the solid lines.

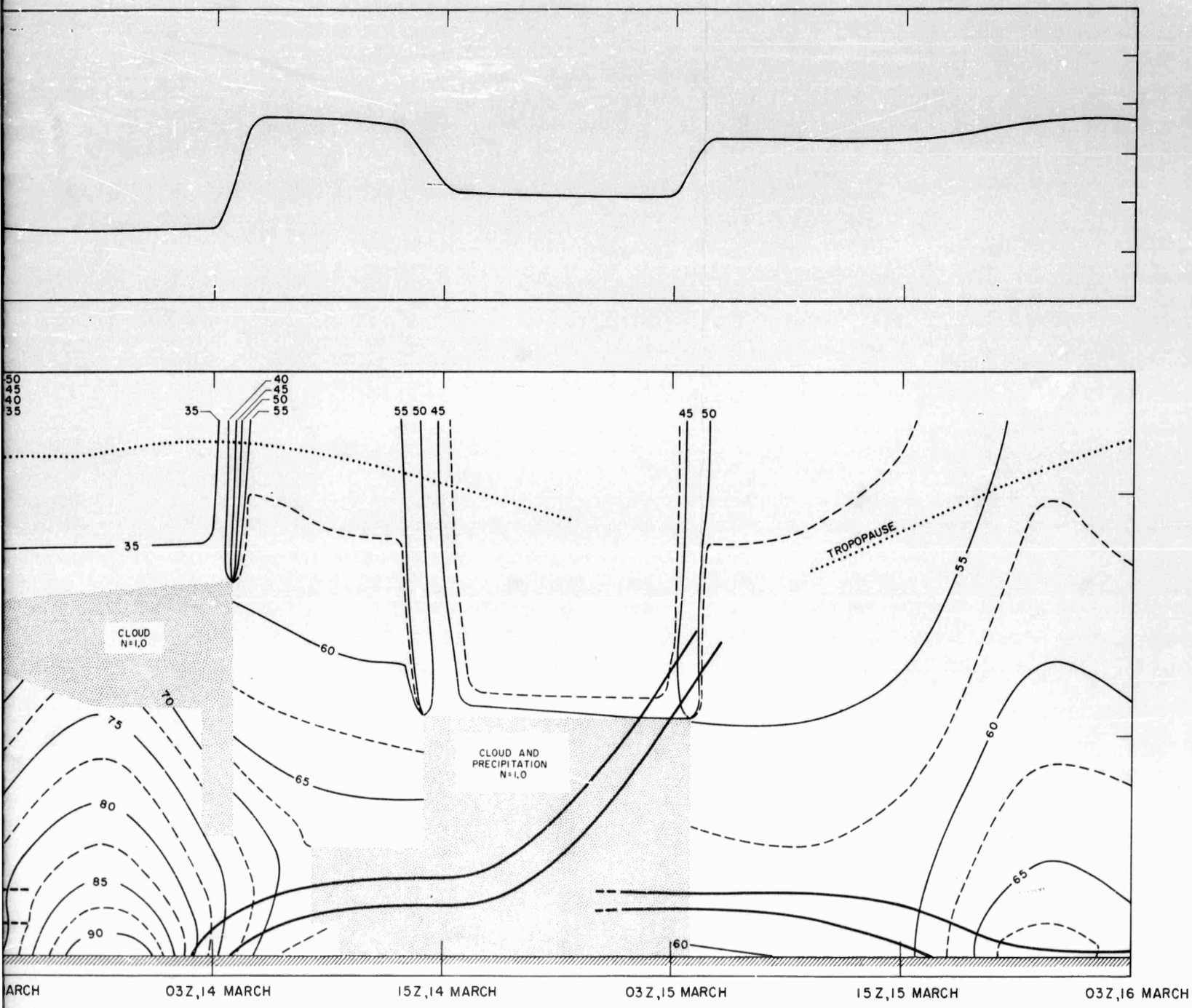

RD—2994—9

FIG. 3

ON OF THE UPWARD LONG-WAVE RADIATIVE FLUX AT OMAHA DURING 12-16 MARCH 1957
ly/3 hr. The dashed lines represent flux values intermediate between the flux values given by the solid lines.

2

The most prominent features of the time section are the marked diurnal variation of F_u and the effect of clouds on the vertical distribution of F_u. The diurnal variation of F_u is in phase with the ground surface temperature such that the maximum at any one level occurs at the time of the midday maximum of the ground surface temperature and the minimum occurs at the time of the early-morning minimum of the surface temperature. This "in phase" time variation of the surface temperature and the vertical distribution of the F_u is the natural consequence of the earth's surface radiating as a black body. It is evident throughout the cloudless troposphere, but the absorption of terrestrial radiation by water vapor somewhat dampens the relationship at the upper levels.

The effect of clouds is to decrease F_u, from clear sky conditions, in the region of the atmosphere above the cloud tops. The largest gradients in the distribution of F_u occur above the edges of the cloud layers and the time rate of change is greatest at those levels nearest to the cloud tops. The uniform distribution of F_u above the clouds reflects the uniformity of the cloud-top temperatures which were assumed to be the same as the free-air temperatures. The black-body assumption for the cloud surfaces results in the vertical distribution of F_u approaching clear-sky conditions with decreasing height of the cloud tops.

With respect to the cloudless atmosphere, there is some change in the magnitudes and in the distribution of F_u between the warm, moist air ahead of the front and the cold, dry polar air behind it. In the former, the flux values are generally larger throughout the air mass because of the higher radiating temperatures [60 to 90 ly $(3\ \mathrm{hr})^{-1}$ as compared to 50 to 70 ly $(3\ \mathrm{hr})^{-1}$ behind the front], and the decrease of F_u with height is greater due to increased absorption brought about by the larger water-vapor content. The polar air mass following the front exhibits the same diurnal variation pattern of F_u as in the pre-frontal air but its drier nature results in greater transparency to terrestrial radiation. The decrease of F_u through a column from the earth's surface to the tropopause is of the order of 7 to 15 ly $(3\ \mathrm{hr})^{-1}$ in the polar air and 15 to 25 ly $(3\ \mathrm{hr})^{-1}$ in the pre-frontal air.

There is no consistent trend in the F_u distribution through inversions. Results of the analysis show both increases and decreases averaging about 2.0 ly $(3\ hr)^{-1}$ from the bases to the tops of inversions, depending on the strength (temperature gradient) and the moisture distribution through the stable layer.

D. UPWARD FLUX AT THE TROPOPAUSE

The time variation of F_u passing through the tropopause level is shown by the curve in the upper section of Fig. 3. The curve essentially represents the time variation of F_u emerging from the top of the atmosphere, since the inclusion of radiative exchanges by the small amount of water vapor and by the other absorbing gases would not significantly alter the configuration of the curve, although the magnitudes may be changed. For instance, Hales and Zdunkowski[4] have computed the radiation fluxes of water vapor, carbon dioxide, and ozone leaving the earth's atmosphere for different types of air masses. While no direct comparison could be made because their computations were made for different atmospheric conditions, their values of radiative flux at the upper limit of the atmosphere are less, by factors of 1.5 to 2.0, than the values of the upward flux at the tropopause obtained in the present study. On the other hand, their results show that the contribution to the total flux leaving the top of the atmosphere by water vapor, carbon dioxide, and ozone are in about the same ratio for all air masses considered.

The relationship between the upward flux at the tropopause and the radiative processes within the atmosphere may be seen from the upper curve and the time cross section of Fig. 3. The largest values of the emergent flux are found in the cloudless atmosphere at the time of the midday maximum of the ground surface temperature. The diurnal variation of the flux still oscillates in phase with the variation of the ground surface temperature but with less magnitude of change than in the lower tropospheric levels. The outstanding feature is the sharp decrease of the outward flux from clear-sky conditions at the periphery of the cloud layers, with a more or less uniform distribution in the area above the cloud top proper. The decrease becomes greater with increasing height

of the cloud tops because of the lower cloud-top temperatures found at the higher levels.

E. DOWNWARD FLUX

The changes in the distribution of the downward flux, F_d, are not as pronounced as the ones depicted by the distribution patterns of F_u. However, some general remarks can be made from the time-sectional analysis of the F_d distribution represented in Fig. 4.

An examination of the field shows, first of all, that F_d increases from the tropopause to the earth's surface. There is no regular diurnal variation of F_d and the variations in the distribution of F_d throughout the day are small compared to the diurnal changes of F_u. Instead of the temperature dependence characterized by the distribution of F_u, the isopleths of F_d parallel the mixing ratio isopleths in the region below 5 km, indicating the close relationship of F_d and the moisture distribution.

At the very high levels, the isopleths of F_d appear to parallel the tropopause. This reflects, at least in part, the restrictions of the computational method, namely, not taking into account the water vapor above the tropopause. On the other hand, the small amount of water vapor in the lower stratosphere would not change the flux values by an appreciable amount. Hales and Zdunkowski[4] found that changing the temperature and moisture distribution at high altitudes in several different ways did not result in any significant changes of the water-vapor flux density.

The presence of a cloud produces a marked change in the vertical distribution of F_d. Its effect is to increase, F_d, relative to clear sky condition, below the cloud layer, with the largest increase occurring just below the cloud base. With increasing optical path length from the cloud base, the cloud effect on the vertical distribution of F_d is reduced and, in the cases of partial cloudiness at 1500Z, 12 March and 0300Z, 13 March, in the time section, it is completely damped out at about 5 km below the cloud layers. The flux that reaches the earth's surface is affected more by clouds with low bases than by those with bases at higher elevations.

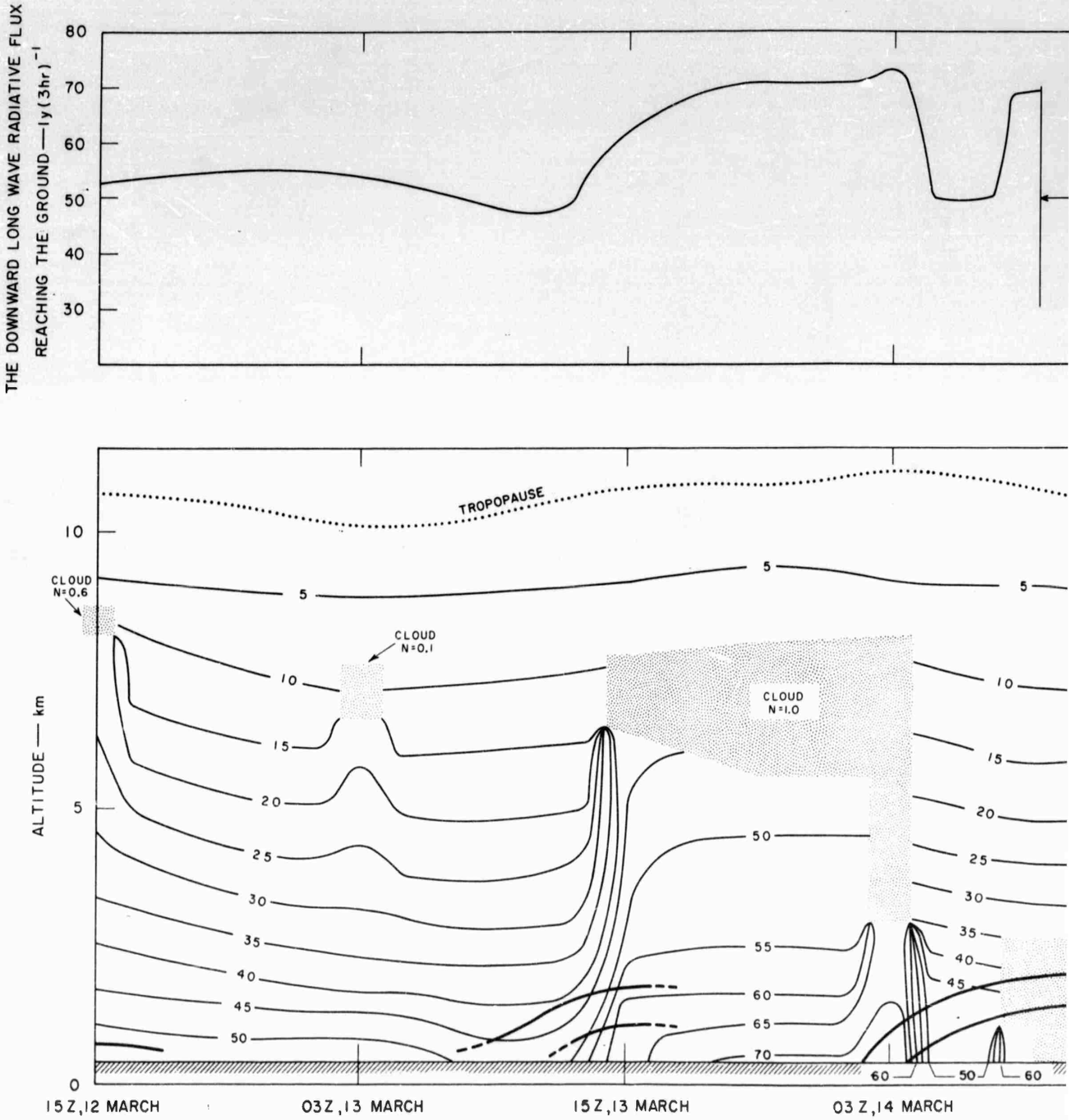

FIG. 4

DISTRIBUTION OF THE DOWNWARD LONG-WAVE RADIATIVI
Units: ly/3 hr

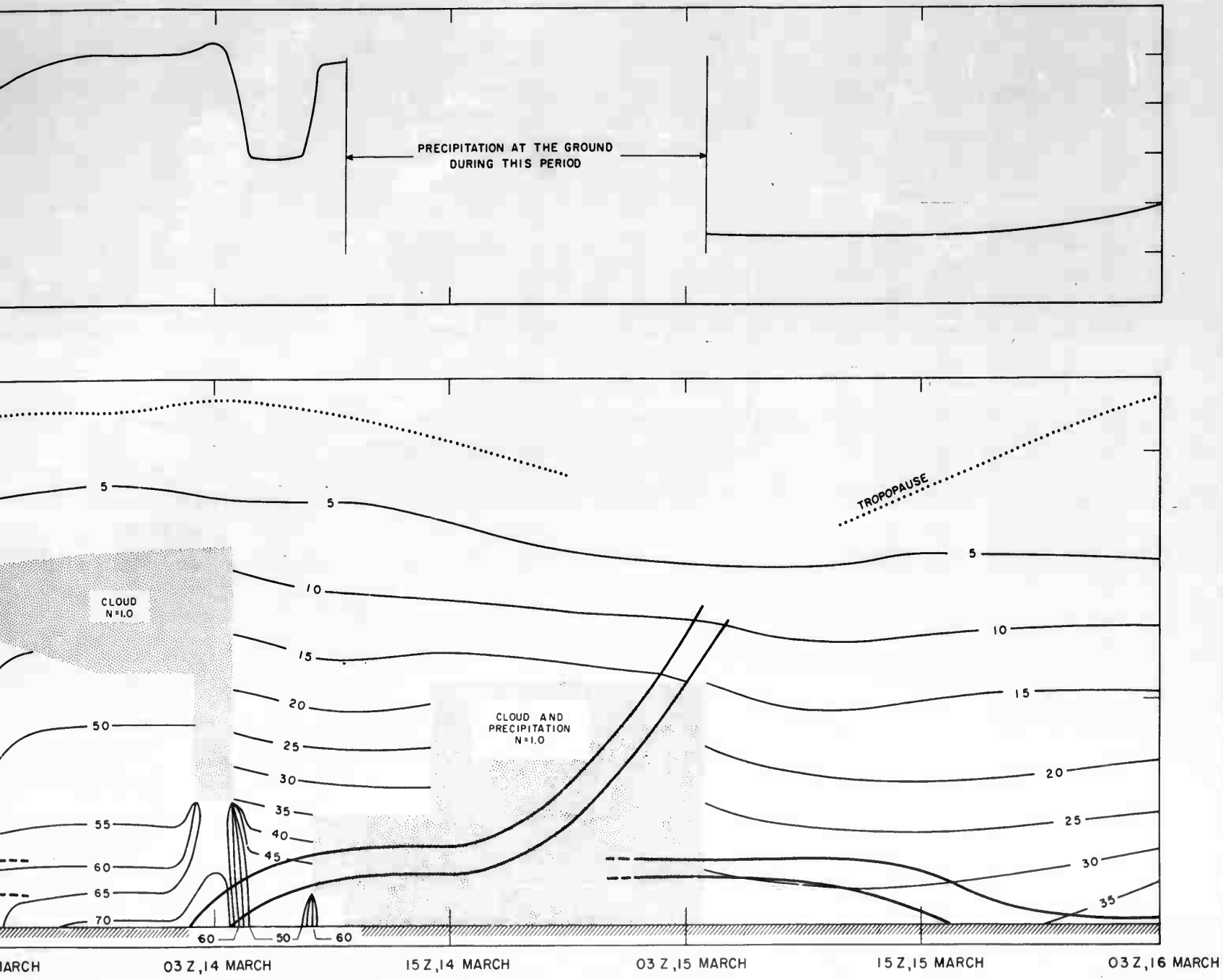

RD—2994—10

FIG. 4

ON OF THE DOWNWARD LONG-WAVE RADIATIVE FLUX AT OMAHA DURING 12-16 MARCH 1957
Units: ly/3 hr

2

Analogous to the change in the upward flux distribution above cloud layers, the largest change in the distribution of F_d occurs at the leading or trailing edges of the cloud bases.

The larger amounts of water vapor in the lower troposphere (< 5 km) result in the rate of change of F_d in the vertical direction being greater there than in the upper troposphere. This effect of increased water vapor is also shown by the difference in the gradients between the air masses. In the moist air ahead of the front, the flux increases by approximately 30 ly $(3\ hr)^{-1}$ from 5 km to the ground, while in the drier air behind it, the increase between the same two levels is a little over 20 ly $(3\ hr)^{-1}$. The difference between the vertical gradients of F_d of the two air masses is not as great for the tropospheric region from the tropopause to the 5-km level.

The computed values of F_d in the clear sky show decreases of 0.5 to 3.0 ly $(3\ hr)^{-1}$ from the bases to the tops of inversions. The small changes of F_d with time mask the decrease of the flux through stable layers, and thus the decrease does not appear in the time section.

F. DOWNWARD FLUX AT THE GROUND

The curve shown in the upper section of Fig. 4 represents the time variation of F_d reaching the ground. In the cloudless sky, the change is not too large over relatively long periods; for instance, between 1500Z, 12 March and 1500Z, 13 March, the flux values for the period vary ± 5 ly $(3\ hr)^{-1}$ from the value at the start of the period. There is partial cloudiness at 1500Z, 12 March and 0300Z, 13 March, but, as mentioned before, the increase of F_d from the cloud bases is dampened by the presence of water vapor in the lower atmosphere and the effect of clouds on F_d is not apparent at the ground. The most significant change is the large increase of F_d brought about by the cloud layer during the period 1500Z, 13 March to 0900Z, 14 March. The gradual change of F_d reaching the earth's surface at the beginning of the period is due to (1) the gradual lowering of the cloud base, thus a gradual change of the radiating temperature of the cloud base, and (2) the decrease of optical path length between the cloud base and the earth's surface over a

relatively extended period. A more abrupt change from overcast to clear sky, and then to overcast conditions, is displayed by the sharp decrease and increase of the curve during 0300Z to 0900Z, 14 March.

G. FLUX DIVERGENCE

The rate of cooling was determined according to the following expression (Elsasser[3]):

$$\left(\frac{\Delta T}{\Delta t}\right)_{3\ hr} = \frac{g}{c_p} \frac{F_{n_1} - F_{n_2}}{|\Delta p|} = 4.1 \frac{F_{n_1} - F_{n_2}}{p_1 - p_2} \qquad (1)$$

where $\underline{g}$ is the acceleration due to gravity, c_p is the specific heat of air at constant pressure, F_{n_1} and p_1 represent the net flux and the pressure, respectively, at the lower boundary of the atmospheric layer, and F_{n_2} and p_2 are the net flux and pressure, respectively, at the upper boundary of the atmospheric layer. The analysis of the rate of cooling for the synoptic situation under investigation is shown in Fig. 5.

The field of flux divergence or rate of cooling displays more cellular patterns than does the upward or downward flux field. It is difficult to establish any regular variations in the cooling patterns or in the vertical distribution of radiative cooling in the clear sky. In a very general sense, there appears to be relatively large cooling in the cloudless atmosphere below 2.5 km; above this level the rate of cooling decreases to about 5 km and then increases to a point below the tropopause level.

The largest rates of cooling are found above the tops of cloud layers and at or above the upper boundaries of inversions and fronts. Even with partial cloudiness, the cooling above cloud layers is increased as compared with either cloudless conditions or with the cooling rates just below the cloud bases. The computed values of the radiative cooling rates above cloud tops range from 0.08°C $(3\ hr)^{-1}$ for 0.6 cloud cover at 1500Z, 12 March, to a maximum of 0.40°C $(3\ hr)^{-1}$ for the overcast at 1500Z, 14 March.

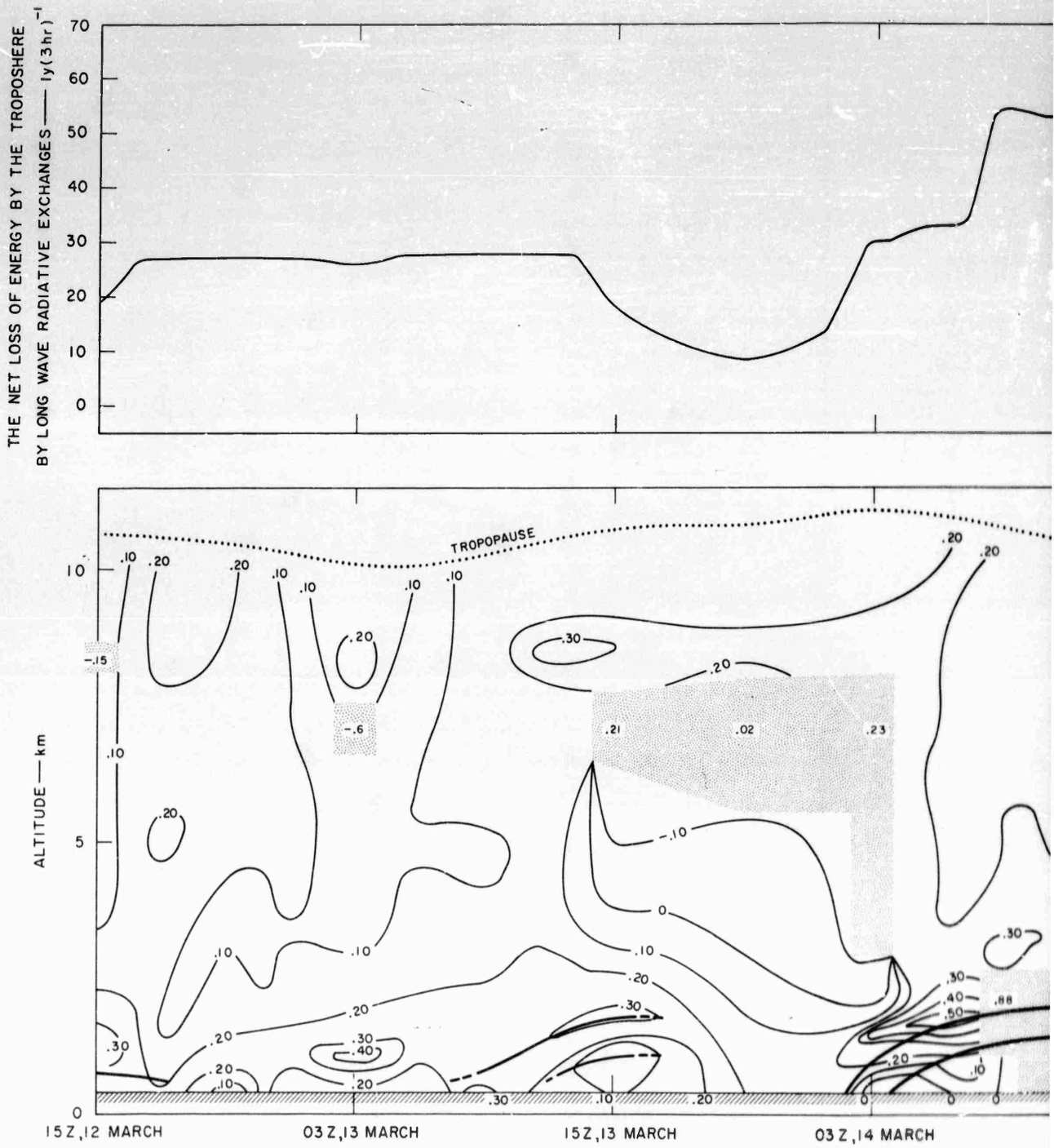

FIG. 5

DISTRIBUTION OF LONG-WAVE FLUX DIVERGENCE (RATE OF CO
Units: °C/3 hr

FIG. 5

F LONG-WAVE FLUX DIVERGENCE (RATE OF COOLING) AT OMAHA DURING 12-16 MARCH 1957
Units: °C/3 hr

2

Below the cloud bases, less cooling takes place through fairly large depths (2 to 4 km) of the troposphere below the clouds. The overcast cover and the low level of the cloud base (higher radiating temperature) result in a region of radiative heating below the cloud layer during the period 1500Z, 13 March to 0300Z, 14 March. A small region of slight heating is also indicated below the low cloud base at 0900Z, 14 March. Below the clouds, the computed temperature changes range from a cooling of 0.08°C $(3\ hr)^{-1}$ to a heating of 0.14°C $(3\ hr)^{-1}$.

The centers of extreme cooling above and near the leading edges of clouds and the sharp gradient and discontinuity at the leading and trailing edge of the cloud base (1500Z, 13 March; 0300Z, 14 March) are due to the assumption of a discontinuity in the flux distribution at the periphery of the cloud layers. However, the general pattern of cooling above the cloud layers and less cooling or heating below the cloud bases are in agreement with the results of Alder.[5] He found maximum radiative cooling to occur 2000 to 3000 ft above cloud tops, and maximum heating below cloud layers to occur at the bases.

The largest rate of cooling [0.50°C $(3\ hr)^{-1}$] is found at the upper boundary of the frontal surface. This is due largely to the large amount of water vapor in the frontal zone, with a rapid decrease of water vapor above. The rate of cooling decreases quite sharply through the frontal layer and near the ground. The lower boundary exhibits a slight heating. In a like manner, increased cooling is seen to take place at or above the tops of inversion layers, with less cooling at the bases. The values range from 0.20 to 0.36°C $(3\ hr)^{-1}$ at the top, to 0.06 to 0.24°C $(3\ hr)^{-1}$ at the bases of the inversions.

Computations were made to determine the rate of cooling within clouds by employing Eq. (1), in which a uniform rate of cooling is assumed to take place throughout the whole depth of the cloud layer. No study of the cooling within a cloud was made other than to get an idea of the order of magnitude. Hoffer[6], using the same expression, found that the rate of cooling within a cloud was approximately a hyperbolic function of the pressure thickness of the cloud layer and that if two clouds were of the same pressure thickness, then the cloud with the base at a higher pressure

cooled more rapidly. The computed values of cooling are shown within each cloud layer in the time section of Fig. 5.

H. LOSS OF ENERGY BY THE TROPOSPHERE

The curve above the time section of Fig. 5 shows the time variation of the net energy loss by long-wave radiative processes from an atmospheric column extending from the earth's surface to the tropopause. The positive values of the curve show that although there may be sub-synoptic regions of long-wave radiative cooling and heating, the net effect of the long-wave radiative processes is the loss of energy by the troposphere. The loss is relatively constant throughout the day in the cloudless atmosphere. The large variations of the energy loss are introduced by the presence of overcast cloud cover.

The minimum amount of energy loss occurs during the period from 1500Z, 13 March to about 0100Z, 14 March. During the period, the net flux, F_n, at the tropopause remains more or less constant, so the variations of energy loss are dependent on what takes place at and below the cloud layers. Between 1500Z and 2100Z on the 13th, the cloud base lowers, thus increasing its radiating temperature and F_d, which reaches the ground. At the same time, the ground surface temperature increases with an accompanying increase of F_u (see Fig. 2). Since F_u at the ground increases more than F_d, F_n is changed so that there is a net gain of energy by the atmosphere at the earth-atmosphere interface, and a decrease of the net energy loss from the troposphere. From 2100Z, 13 March to about 0100Z 14 March, the cloud base remains at a constant level, as does the cloud top, but the decrease of the ground surface temperature results in F_u and F_n at the earth's surface being decreased. Therefore, during this period, there is less net energy transferred to the atmosphere from the ground, or an increase in the net loss of energy by the troposphere.

The maximum of energy loss by the troposphere occurs from 0900 to 1300Z, 14 March. At 0900Z, the low height of the cloud top results in a relatively high radiating temperature and a fairly large value of F_u and F_n at the tropopause. Below the cloud layer the temperature of the cloud base is higher than that of the ground surface and results in F_n

at the earth's surface being directed from the atmosphere to the ground instead of vice-versa, as is generally the case. This loss of energy at 0900Z is comparatively large. The black-body assumption for the cloud-precipitation combination results in the lowering of the black-body surface (cloud base) to the ground during the period from about 1000Z to 1300Z. The consequent change in the net energy loss by the troposphere is a slight decrease from the amount at 0900Z.

I. EFFECTS OF GROUND SURFACE TEMPERATURE

It was assumed in the present study that the radiating temperature of the ground surface was equivalent to the reported surface air temperature given in the regular meteorological observation. This has two consequences. First, it is known from observations (Geiger[7], Lettau and Davidson[8]) that the temperature of the earth's surface can differ appreciably from the temperature of the air layer next to it. Since the flux of radiant energy emitted by the earth's surface is proportional to the fourth power of its absolute temperature, the amount of energy computed by the application of the assumption above may result in a significant error. Computations of fluxes were made to determine the probable error that may arise from neglecting any air-ground temperature differences. The changes in the vertical distributions of F_u and F_n for 5°C differences of the ground temperature from that assumed in the study are shown in Fig. 6. The change in F_u and F_n due to different radiating temperatures of the ground is greatest at the earth-atmosphere interface, decreases slightly with height in the lowest air layers, and is more or less constant throughout the tropospheric levels above. The curves show that if the ground temperature is greater than the assumed temperature, the radiant flux emitted by the earth's surface is increased by approximately eight percent for each 5°C and is decreased by nearly the same amount when the ground temperature is less than the assumed temperature. These variations of F_u result in F_n at the interface being increased or decreased by about twenty-five percent for each 5°C increment of temperature difference.

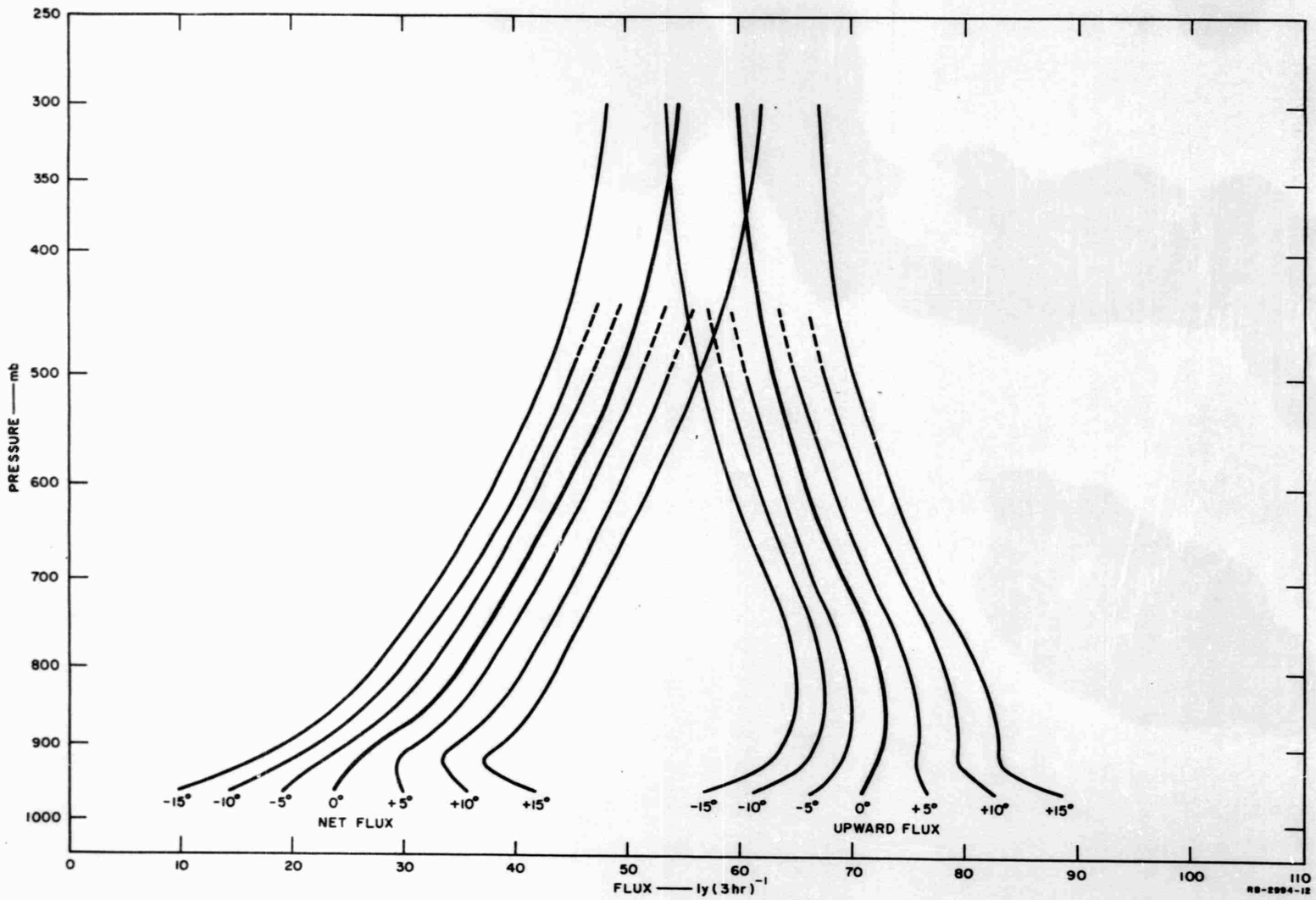

FIG. 6

THE EFFECT OF THE GROUND SURFACE TEMPERATURE ON THE UPWARD AND NET LONG-WAVE FLUX DISTRIBUTIONS

At the middle and upper tropospheric levels, including the tropopause, F_u and F_n are changed in the same sense as mentioned above, but the changes are only 4% to 5% for each 5°C temperature difference.

The second consequence introduced by assuming the ground surface temperature to be the same as the reported surface air temperature is that of a phase displacement of the diurnal oscillation. Generally, the phase difference between the diurnal variations of the two temperatures is of the order of only an hour or so. This corresponds to a shift of the patterns by a like amount in the time-section representation, while the distribution patterns themselves are otherwise unaffected by the shift.

J. SUMMARY

The case study of the long-wave terrestrial radiation regime shows that the distribution of the upward long-wave flux in the clear atmosphere decreases with height and has a time variation that is in phase with the diurnal oscillation of the ground surface temperature. The downward flux also, during cloudless conditions, increases from the tropopause to the earth's surface but does not exhibit any regular diurnal variations and, in addition, its changes with time are small compared to those of the upward flux. The most important feature for producing pronounced changes in the distributions of the fluxes is the presence of clouds. The effect of clouds is to reduce the upward flux, from clear sky conditions, in the region above the cloud tops. The black-body assumption for the cloud surfaces results in the distribution of the upward flux above the cloud tops to approach that of cloudless conditions with decreasing height of the cloud tops. The downward flux is increased by clouds in the region below the cloud bases. The flux reaching the ground is decreased with increasing cloud height, because of lower cloud-base temperature and more absorption by water vapor. The time-varying field of flux divergence is of a more cellular nature than either the upward or downward-flux field. In the cloudless atmosphere, the rate of cooling is relatively large in the air layers below about 2.5 km, decreasing above that level to the middle troposphere, and then increasing to the tropopause. Maxima of cooling occur above cloud layers and at or above the upper boundaries of

inversions and fronts. Less cooling or heating, depending on the synoptic conditions, takes place in the region below cloud layers and at the lower boundaries of inversions and fronts. The contribution of the long-wave radiative exchanges to the over-all energy budget is a net loss of energy by the atmosphere.

V THE SHORT-WAVE SOLAR RADIATION REGIME

A. GENERAL

The main processes effecting the distribution of solar radiant energy in the atmosphere are (1) scattering by the molecules of the air, (2) reflection from ground or clouds, (3) absorption by atmospheric constituents such as ozone and water vapor, and (4) scattering and absorption by particles such as haze and dust. For the present case study, the first two of these were studied by the use of the exact theory of radiative transfer, as originally derived by Chandrasekhar[9] and extensively applied by Sekera and collaborators.[10] The latest information on the distribution of ozone was used to determine the rate of heating by ultraviolet absorption by ozone, and an empirical method derived by Korb, et al.,[11] was applied for determining water-vapor absorption. The effects of haze and dust were evaluated by means of a three-layered atmospheric model adapted from Waldram's[12] measurements.

Quantitative values of the total contribution and the diurnal variation of each process were computed for the selected synoptic situation at Omaha. The methods and results are discussed in the following sections.

B. MOLECULAR SCATTERING AND SURFACE REFLECTIONS

1. Introduction

Solar radiation is returned to space by the earth-atmosphere system principally through four interdependent processes, namely (1) scattering by gaseous molecules of the air, (2) reflection from the underlying land or water surface, (3) scattering by liquid water droplets composing clouds, and (4) scattering by aerosol particles such as haze and dust. The contributions of the first three of these processes are considered quantitatively in this section. First the combined effects of molecular scattering and surface reflection for a cloudless and dust-free atmosphere are evaluated for an idealized atmospheric model. Then, the reflectance

of a cloud-plus-Rayleigh-atmosphere system, in which the top of a uniform cloud deck of reflectance A = 0.50 is located at various altitudes, is similarly examined.

The model atmosphere is one of finite optical thickness in the vertical, homogeneous and of infinite extent in the horizontal, and non-absorbing. The atmosphere is bounded on top by a perfect vacuum and at the bottom by a diffusely reflecting surface of arbitrarily set reflectivity A such that $0 \leq A \leq 1$. For the case of clouds, the lower boundary is the top of the cloud deck; otherwise it is assumed to be a diffusely reflecting surface at sea level.

2. Method of Calculation

The exact solution of the general equation of radiative transfer, as obtained by Chandrasekhar,[9] was used for the calculations. The atmospheric model is characterized by the normal optical thickness

$$\tau(\nu,z) = \int_z^{\infty} \beta_\nu dz \tag{2}$$

where ν is the frequency of the radiation, β_ν is the frequency-dependent volume-scattering coefficient, and z is the vertical coordinate. We assume πF_o units of energy per unit frequency interval and unit time are incident on a unit area normal to the direction of propagation of the parallel radiation at the top of the atmosphere, the direction being specified by the solar zenith angle θ_o and azimuth ϕ_o. The intensity, I, of the scattered radiation emerging from the top of the atmosphere is a function of the nadir angle θ and azimuth ϕ. Then the total upward flux D_ν through a unit horizontal area per unit frequency interval and unit time, is given by an integration of intensity over the downward hemisphere:

$$D_\nu = \int_o^{2\pi} \int_o^{\frac{\pi}{2}} I_\nu(\theta,\phi) \sin\theta \cos\theta \, d\theta d\phi \ . \tag{3}$$

If we assume that the underlying surface, be it soil, vegetation, or other material, reflects isotropically a fixed fraction, A, of the radiation incident on it, then the upward stream is composed of both scattered and surface-reflected radiation. When the integration of Eq. (3) is carried out for this case (see Coulson[13]), we obtain

$$D_\nu(\tau,\mu_o,A) = \pi F_o \mu_o \left[1 - \left(\frac{\gamma_\ell + \gamma_r}{2}\right)\left(\frac{1 - A}{1 - A\bar{s}}\right)\right] . \tag{4}$$

Here $\mu_o = \cos \theta_o$, and $\bar{s}$ is a known function of only the optical thickness. The functions γ_ℓ and γ_r, derived originally by Chandrasekhar,[9] are functions of both μ_o and τ. Numerical values of them are available. For this work the following tabulations were used:

Sekera and Blanch:[14]	τ =	1.0, 0.25, 0.15
Sekera and Ashburn:[15]	τ =	0.10, 0.05, 0.02, 0.01, 0.003, 0.001
Chandrasekhar and Elbert:[16]	τ =	0.50

Sekera and Ashburn reported some computational difficulties for $\tau = 0.003$ and $\tau = 0.001$, and there is some question about the accuracy of their tabulated values. The comparisons given by those authors indicate, however, that the final values are reliable to about three places, which is sufficient for the present computations, and the results obtained here appear to be internally consistent throughout. Their tabulations were used, therefore, without alteration.

3. Effect of Surface Reflectivity

It was found in a previous investigation (Coulson[13]), that the reflectance of the atmospheric model is critically dependent on the reflectivity of the underlying surface. In order to define the dependence more explicitly, the monochromatic reflectance, given by

$$R_\nu = \frac{D_\nu}{\pi F_{o\nu} \mu_o} \tag{5}$$

was computed for eight different values of surface reflectivity for a number of optical thicknesses and solar zenith angles. Curves of R_ν as a function of surface reflectivity A for large optical thickness are

given in Fig. 7, the parameter being solar zenith angle θ_o. The dashed curve represents the reflectance the system would have if the atmosphere were not present. It is seen that the atmosphere itself scatters back a large portion of this short-wavelength radiation (λ = 3120 Å),* particularly at the larger solar zenith angles. A value of $R_\nu = 0.75$ is found for A = 0 for the largest θ_o, and the reflectance of the system is everywhere greater than 0.34. Even here, however, the surface reflected radiation is predominant for large values of A. For A = 1.0 all of the curves must converge at the point $R_\nu = 1.0$, since we assume a non-absorbing atmosphere.

The equivalent curves for moderate optical thickness ($\tau = 0.10$) and for very small optical thickness ($\tau = 0.001$) are shown by Figs. 8 and 9, corresponding to the yellow (5460Å) and infrared (17,000 Å), respectively. The very minor role played by atmospheric scattering compared to surface reflection at the longer wavelengths is evident. This wavelength dependence is a feature of considerable practical importance in the design and operation of radiation-sensing satellites.

A complete tabulation of the monochromatic reflectance R_ν of the atmosphere-surface system for ten different optical thicknesses, from which those of Figs. 7, 8, and 9 were selected, is included as an Appendix of this report.

4. Effect of Solar Angle

The reflectance of the surface-atmosphere system is strongly affected by the angle of incidence θ_o of the incoming radiation. Curves of system reflectance as a function of $\mu_o = \cos \theta_o$ for four different values of surface reflectivity are reproduced in Fig. 10. The data were obtained by an integration of Eq. (5) with wavelength, the incident energy being assumed to have the same spectral distribution as that of extra-terrestrial sunlight. The spectral range covered is 3100 Å $\leq \lambda \leq$ 25,000 Å, representing

* The conversions of optical thickness to wavelength are for z = 0 (sea level) unless otherwise specified.

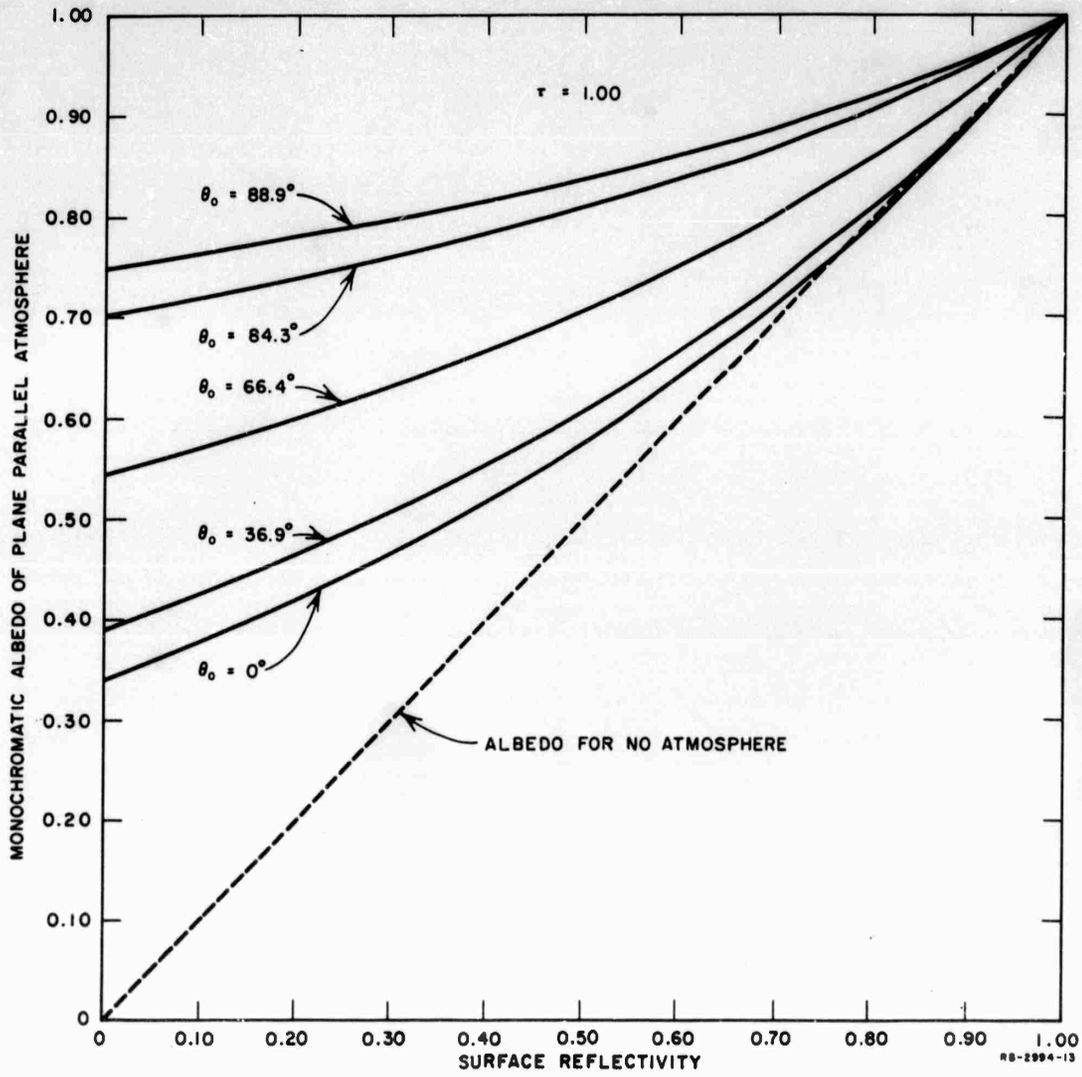

FIG. 7

MONOCHROMATIC REFLECTANCE OF MODEL ATMOSPHERE-PLUS-SURFACE SYSTEM AS A FUNCTION OF SURFACE REFLECTIVITY FOR OPTICAL THICKNESS $\tau = 1.00$ FOR FIVE DIFFERENT SOLAR ZENITH ANGLES

$\tau = 1.00$, corresponding to wavelength $\lambda = 3120$Å at sea level.

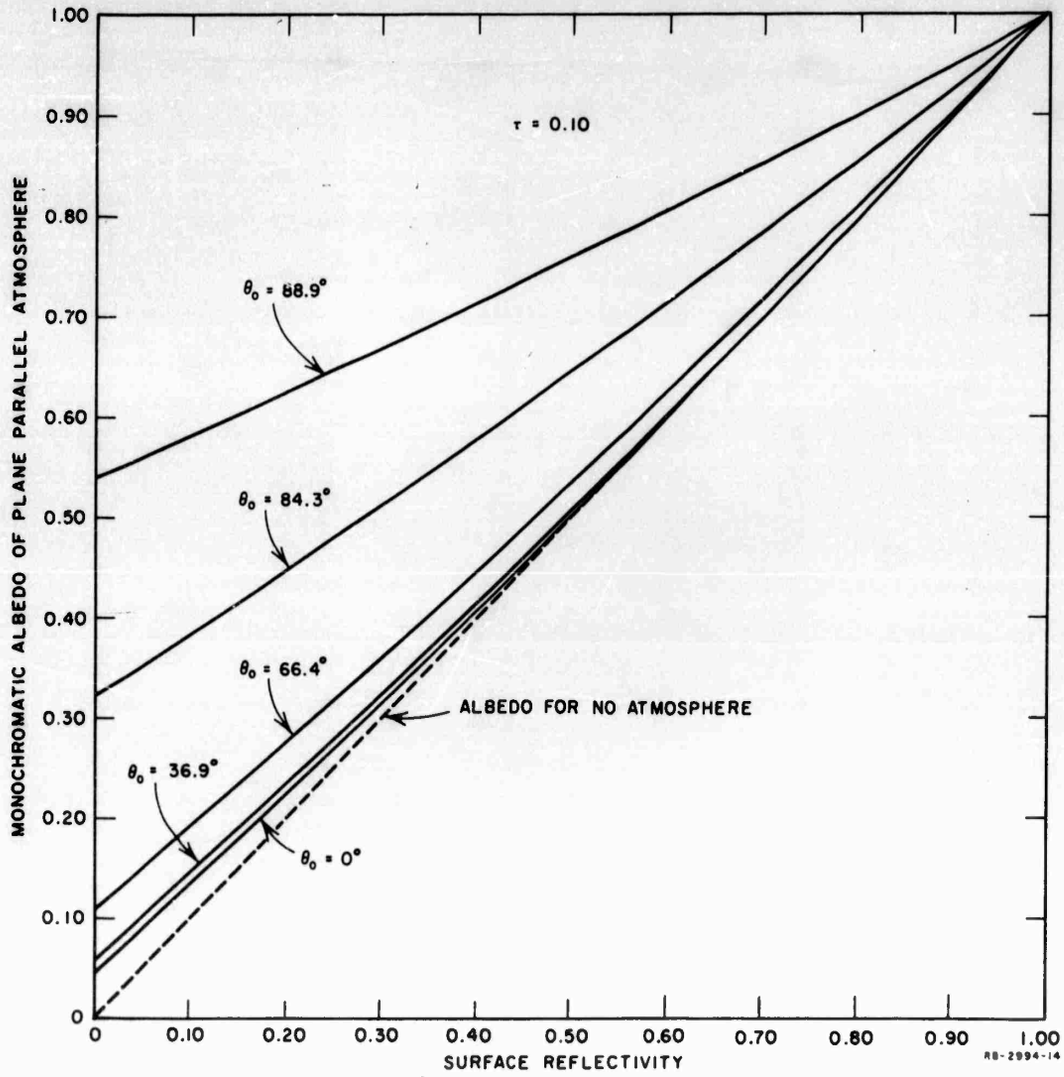

FIG. 8

MONOCHROMATIC REFLECTANCE OF MODEL ATMOSPHERE-PLUS-SURFACE SYSTEM AS A FUNCTION OF SURFACE REFLECTIVITY FOR OPTICAL THICKNESS $\tau = 0.10$ FOR FIVE DIFFERENT SOLAR ZENITH ANGLES
$\tau = 0.10$, corresponding to wavelength $\lambda = 5460$Å.

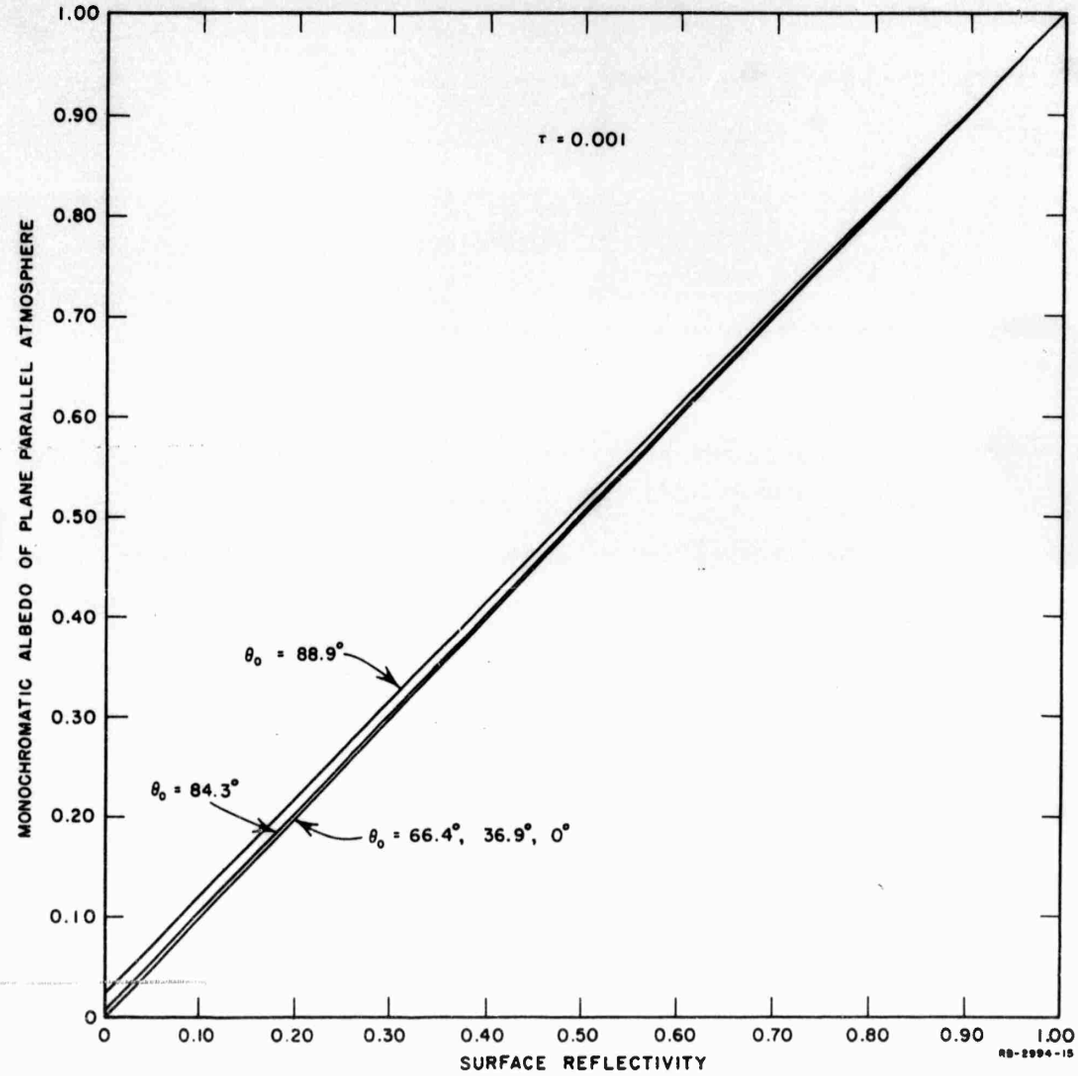

FIG. 9

MONOCHROMATIC REFLECTANCE OF MODEL ATMOSPHERE-PLUS-SURFACE SYSTEM AS A FUNCTION OF SURFACE REFLECTIVITY FOR OPTICAL THICKNESS $\tau = 0.001$ FOR FIVE DIFFERENT SOLAR ZENITH ANGLES

$\tau = 0.001$, corresponding to wavelength $\tau = 17{,}000$Å.

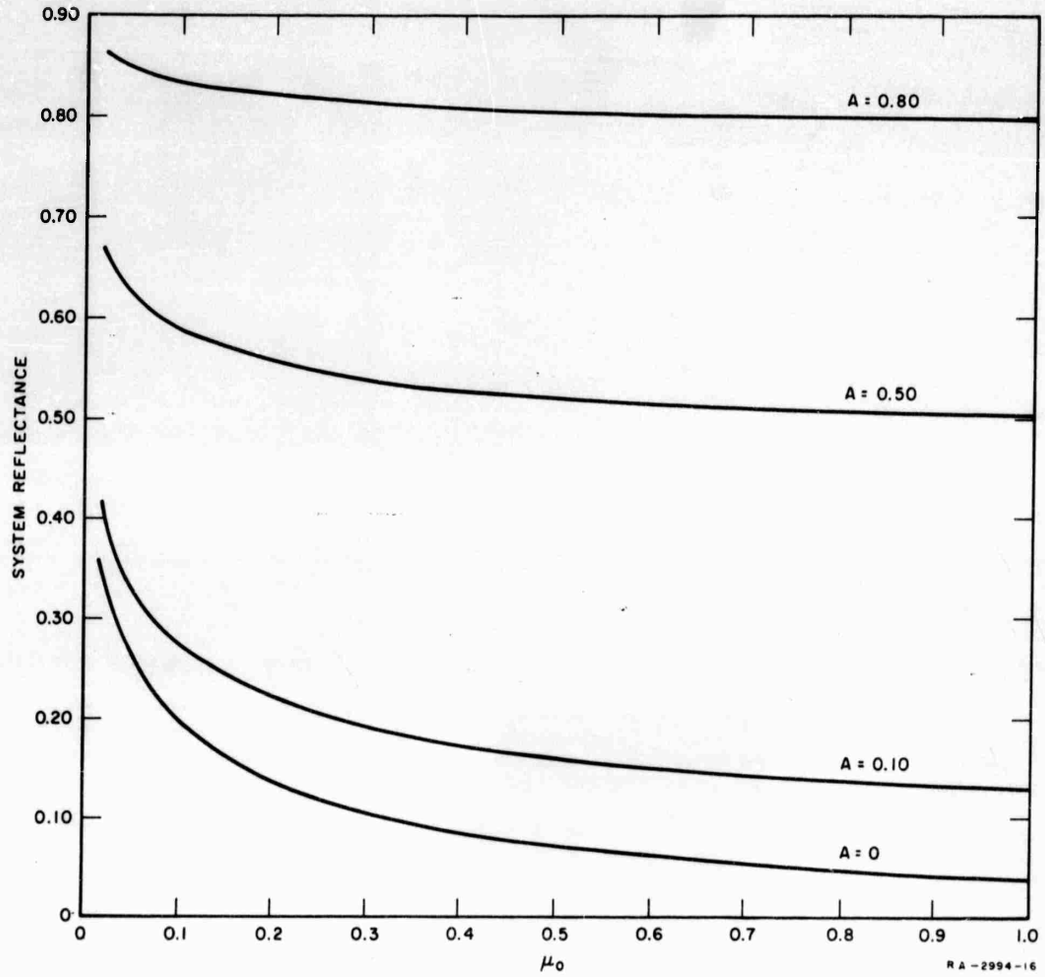

FIG. 10

REFLECTANCE OF MODEL ATMOSPHERE-PLUS-SURFACE SYSTEM AS A FUNCTION OF COSINE OF SOLAR ZENITH ANGLE μ_0 FOR SPECTRAL INTERVAL 3100Å $\leq \lambda \leq$ 25,000Å FOR DIFFERENT VALUES OF SURFACE REFLECTIVITY

about 95% of the incident solar energy, and integration was by the trapezoidal rule. The strong dependence of system reflectance on solar position at small values of μ_0, particularly pronounced for small values of A, results from backscatter, both primary and multiple, in the long atmospheric pathlengths existing for large solar zenith distances. The amount of backscatter decreases rapidly with increasing μ_0, however, resulting in small changes of system reflectance for μ_0, greater than about 0.40. The dominating influence of surface reflectivity is evident in the curves.

To show the effects of the different spectral regions, the solar spectral range was broken into the ultraviolet (3100 Å $\leq \lambda \leq$ 4000 Å), visible (4000 Å $\leq \lambda \leq$ 7000 Å), and infrared (7000 Å $\leq \lambda \leq$ 25,000 Å), and reflectance curves were determined for each region as a function of solar angle. The results are shown in Fig. 11 for four values of A. It is seen that the reflectance characteristics change significantly from the ultraviolet to the infrared. A relatively strong dependence on solar

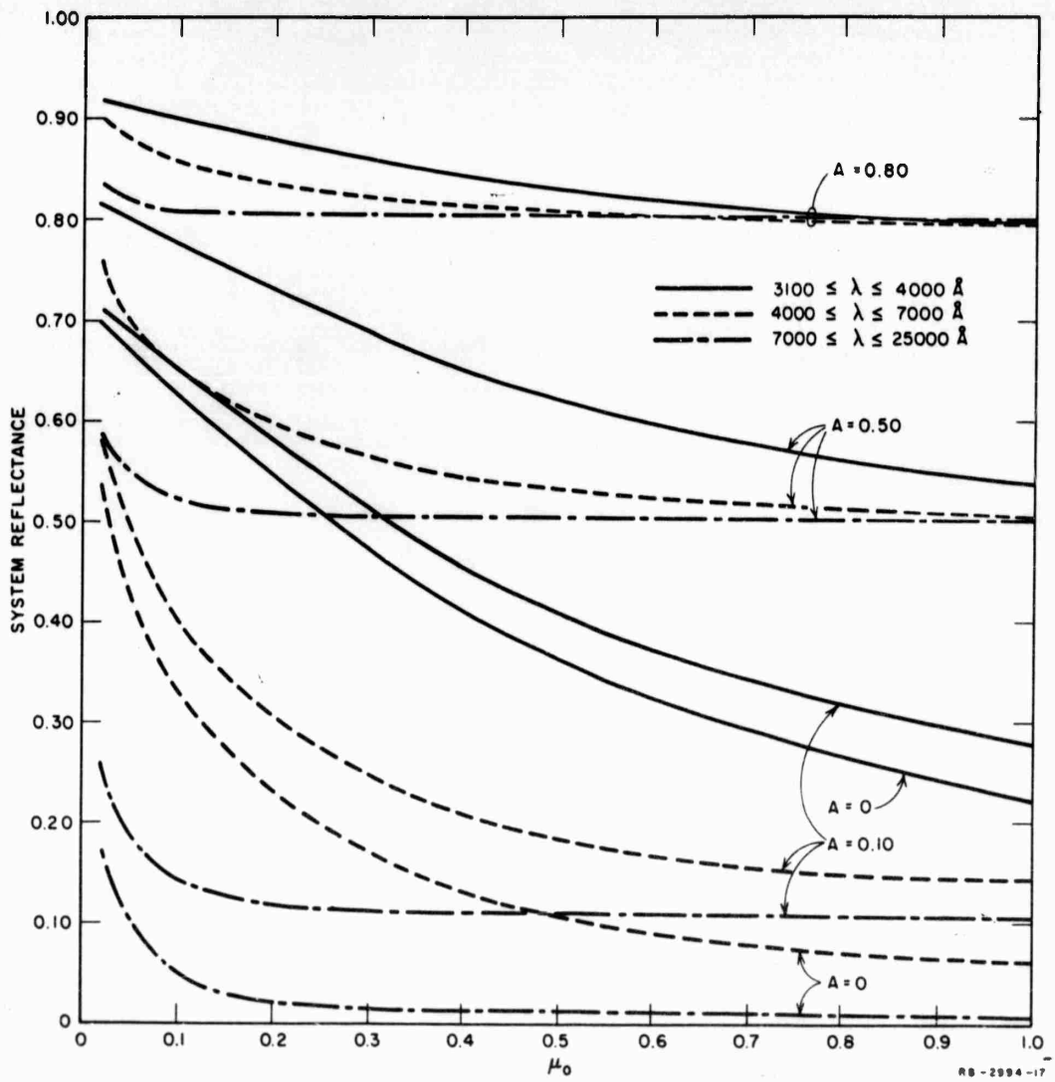

FIG. 11

REFLECTANCE OF MODEL ATMOSPHERE-PLUS-SURFACE SYSTEM AS A FUNCTION OF COSINE OF SOLAR ZENITH ANGLE μ_0, WITH SPECTRUM DIVIDED INTO ULTRAVIOLET (3100Å < λ < 4000Å), VISIBLE (4000Å < λ < 7000Å), AND INFRARED (7000Å < λ < 25,000Å)

angle continues throughout for the ultraviolet, the one exception being for A = 0.80, but nowhere do the slopes show extreme values. In the infrared, however, the rapid decrease of reflectance with decreasing solar zenith angle shows that Rayleigh scattering of the long waves is significant only for very long atmospheric pathlengths. For A = 0.80 the system is a good reflector for all spectral regions.

5. Variation with Altitude of Reflecting Surface

Because of the dependence of optical thickness on altitude as well as on wavelength, the system reflectivity is a function of the altitude z_s of the reflecting surface. The discussion so far has been for $z_s = 0$. Similar computations have been made for a surface of reflectivity A located at altitudes of z_s = 2 km, 5 km, 10 km, 20 km, and ∞. The last case corresponds to the surface being above the atmosphere, so that the system reflectance is identical to A. Again, the incident flux and spectral distribution of extra-terrestrial sunlight is assumed, and the range covered is 3100 Å $\leq \lambda \leq$ 25,000 Å. The altitude-wavelength dependence for a given optical thickness was taken from Deirmendjian.[17] Computations were made for a single reflectivity, A = 0.50 having been chosen as a reasonable value for the reflectivity of an actual cloud.

The upward flux as a function of wavelength for $\theta_0 = 66.4°$ is shown in Fig. 12, for the three altitudes z_s = 0, 5 km, ∞. Ordinate values for the curve $z_s = \infty$ are simply one-half those of the incident radiation, since the atmospheric effect is nil for this case. Comparison of the curves shows that the effect of atmospheric scattering by the air above a highly reflecting cloud top is minor, or completely negligible, at this sun elevation for the entire region $\lambda >$ 8000 Å. In the visible and ultraviolet, however, the dependence of upward flux on z_s is important, the value being 41% higher for $z_s = 0$ than for $z_s = \infty$ at λ = 3100 Å. The effect is less at smaller solar zenith angles, but the corresponding increment is still 13% for $\theta_0 = 0$.

The case for $\theta_0 = 88.9°$ is given by Fig. 13, in which curves for five different values of z_s are included. A major change with z_s is seen here, and the influence extends well into the infrared. Even for

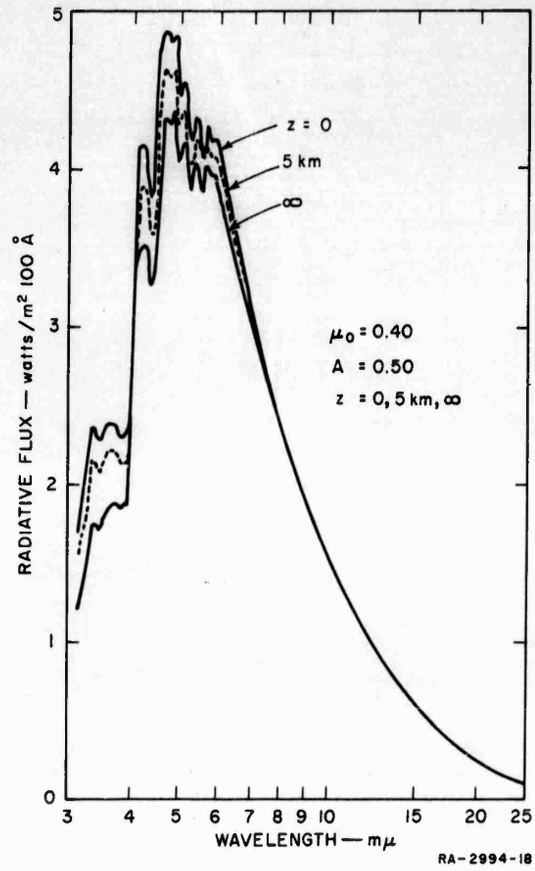

FIG. 12

UPWARD FLUX FROM THE TOP OF MODEL ATMOSPHERE AS A FUNCTION OF WAVELENGTH FOR SOLAR ZENITH ANGLE 66.4° WITH A SURFACE OF REFLECTIVITY 0.50 LOCATED AT DIFFERENT ALTITUDES

z_s = 20 km, atmospheric scattering increases the upward flux by 46% over its value for $z_s = \infty$ at λ = 3100 Å.

If the spectral range is again divided into ultraviolet, visible, and infrared regions and the angular integrations described above are performed, it is a simple matter to compute the reflectance of the system as a function of μ_0. The result of this procedure for the ultraviolet, for A = 0.50, is shown in Fig. 14. For the sun near the horizon (θ_0 = 88.9°) the reflectance of the system changes slowly with z_s, decreasing only to 0.70 for z_s = 20 km. The region of maximum sensitivity,

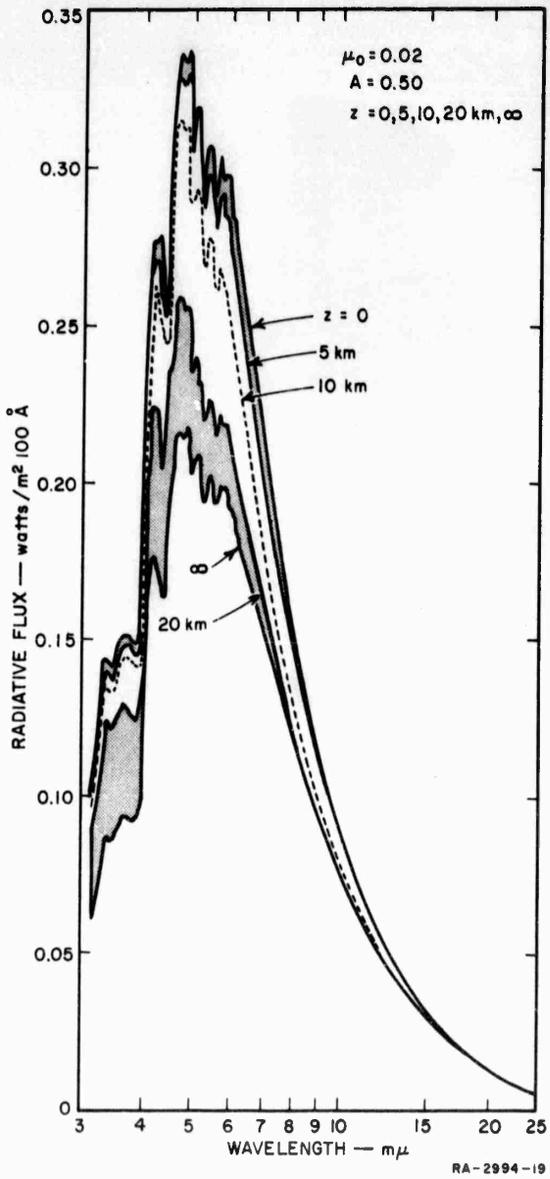

FIG. 13

UPWARD FLUX FROM THE TOP OF MODEL ATMOSPHERE AS A FUNCTION OF WAVELENGTH FOR SOLAR ZENITH ANGLE 88.9° WITH A SURFACE OF REFLECTIVITY 0.50 LOCATED AT DIFFERENT ALTITUDES

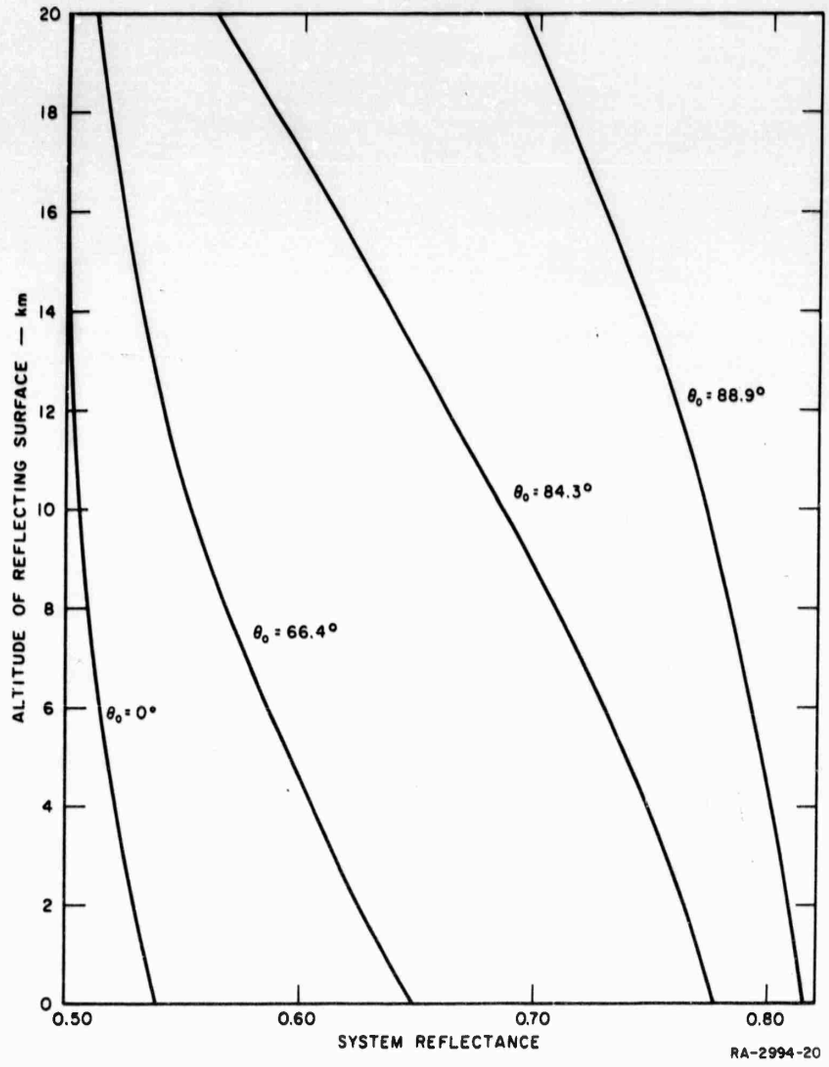

FIG. 14

SYSTEM REFLECTANCE AS A FUNCTION OF ALTITUDE OF SURFACE OF REFLECTIVITY 0.50, FOR THE ULTRAVIOLET (3100Å < λ < 4000A) AT FOUR DIFFERENT SOLAR ZENITH ANGLES

indicated by the greatest slope of the curves, decreases in altitude with decreasing solar angle. For small zenith angles the sensitivity is small at all altitudes because of the dominance of surface-reflected radiation.

The equivalent curves for the visible and infrared are reproduced in Fig. 15. The dominant role in surface-reflected radiation makes the reflectance insensitive to z_s for the infrared, but for the visible a large dependence is indicated at low sun elevations.

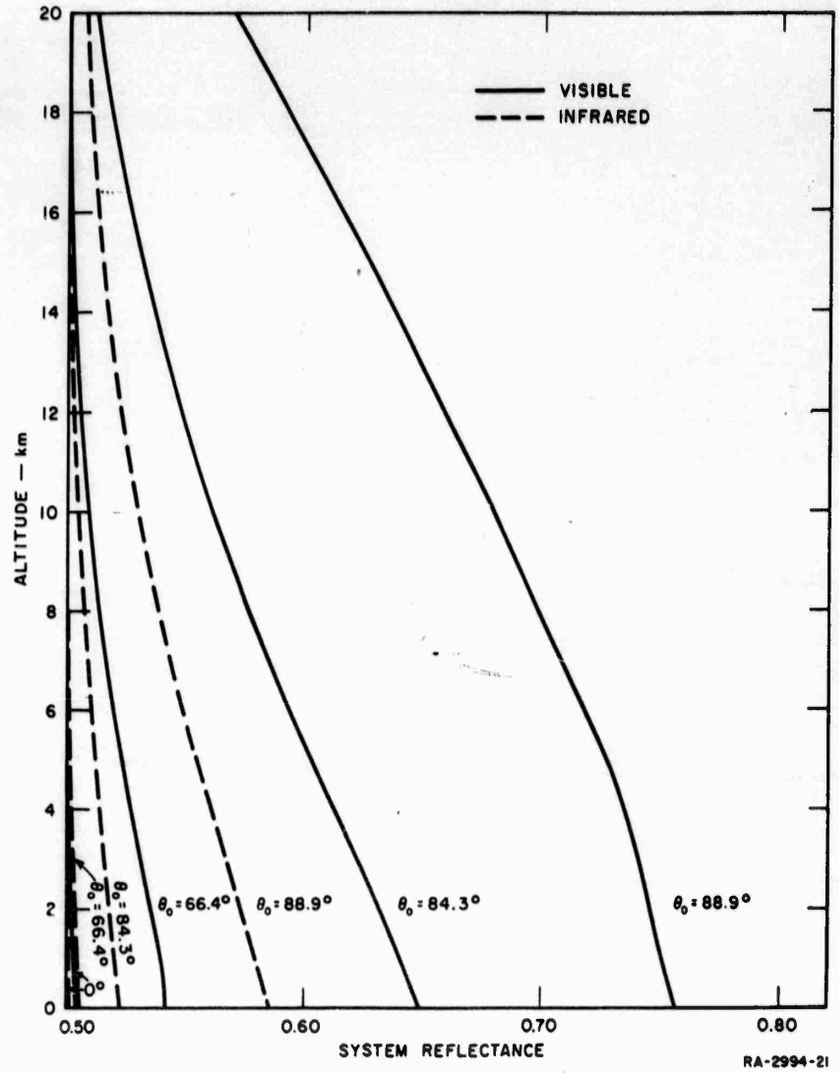

FIG. 15

SYSTEM REFLECTANCE AS A FUNCTION OF ALTITUDE OF SURFACE OF REFLECTIVITY 0.50, FOR VISIBLE (4000Å < λ < 7000Å) AND INFRARED (7000Å < λ < 25,000Å) AT FOUR DIFFERENT SOLAR ZENITH ANGLES

6. Discussion

From a practical standpoint, it appears that the wavelength dependence of the light emerging from the top of the atmosphere could be used as a measure of the amount of Rayleigh scattering occurring above a cloud top, or, equivalently, the altitude of the cloud top. In order to assess the possibilities, we should take another look at the assumptions underlying these computations.

First, the reflectance of the cloud top is assumed to be 0.50, independent of wavelength. This value of A was arbitrarily chosen as being reasonable, and not as realistic for any given cloud type, but the character of the curves would persist through a reasonable change of A. Furthermore, wavelength independence of A is not required, but only that the functional dependence be known. From theory, one would expect the wavelength dependence of cloud-droplet scattering to be minimal, since the cloud droplets are well into the Mie scattering domain and consist of a distribution of sizes. This is qualitatively borne out for the visible spectrum by the lack of color in cloud-reflected or transmitted sunlight.

The second assumption, that of a horizontally stratified atmosphere resting on a flat earth, introduces an artificiality that must be removed for hemispheric flux measurements from a satellite, to be useful for cloud height determination. Approximation of atmospheric sphericity by many plane areas of different orientations will probably be satisfactory, however, for present purposes.

Third, radiative scattering by dust and haze has not been considered here. A first approximation to the effect could be obtained by the method suggested by Sekera[18] if the physical properties of the particles and their spatial distribution were known. These quantities, however, are extremely variable in the atmosphere, and data are sparse. Pending further work in this area, the effects of such atmospheric turbidity must serve only to increase the uncertainties inherent in the method.

It would appear from such preliminary considerations that this method of cloud-height determination is sufficiently attractive to merit more detailed developmental work.

Two other possibilities for cloud-height determination by light-scattering measurements should, perhaps, be mentioned: (1) Instead of integrating the intensity over the hemispheric solid angle, as suggested above, there are some important advantages in measuring the intensity of the light scattered into a small solid angle in a given direction. (2) The extremely different polarizing properties of air molecules and

cloud particles might be used to determine the optical thickness of the air overlying a cloud deck, and hence the height of the cloud top.

7. Application to Synoptic Situation

The above results were applied to the particular synoptic situation under investigation, yielding values of the upward flux of solar energy from the top of the atmosphere and the energy absorbed by the atmosphere-ground system at Omaha, as a function of time. Clouds were assumed to reflect 0.50 of the radiation incident on them, and for partly cloudy sky the data were weighted by the fractional sky cover. The reflectivity of the snow-covered ground was taken as $A = 0.80$, and for bare ground $A = 0.10$. No correction was made for the wavelength regions $\lambda > 25{,}000$ Å and $\lambda < 3100$ Å. Since those combined regions contain only about 5% of the solar energy and constitute both strongly scattered and weakly scattered portions, their effects on the curves would be small.

The solid curves of Fig. 16 show the flux of solar energy returned to space by the atmosphere-ground system at Omaha for the four days March 12-15, 1957, while the dashed curves give the energy absorbed by the ground during the same period. The great effect of surface reflectivity is evident, being particularly pronounced for the case of snow cover during the forenoon of March 15. Cloud height has a minor effect as long as the cloud reflectivity is independent of height. This can be seen by comparing the curves of March 13 (cloud top, 8300 m) with those of March 14 (cloud top, 3000 m and 5700 m).

C. ABSORPTION BY WATER VAPOR

The absorption of solar energy by the usual amounts of atmospheric water vapor are not unimportant in the atmospheric heat balance. Korb, et al.,[11] found the amount of absorbed energy to vary from 178 ly/day for high water vapor content and high incident energy to zero for the polar night. Values of 5 to 10% of the incident energy were common. Kimball[19] gave values of 6 to 12% for moderate water-vapor pathlengths.

By processing the absorption data of Howard, Burch, and Williams,[20] Korb[11] found that the amount of solar energy E_V absorbed by water vapor in the entire thickness of the atmosphere can be approximated by

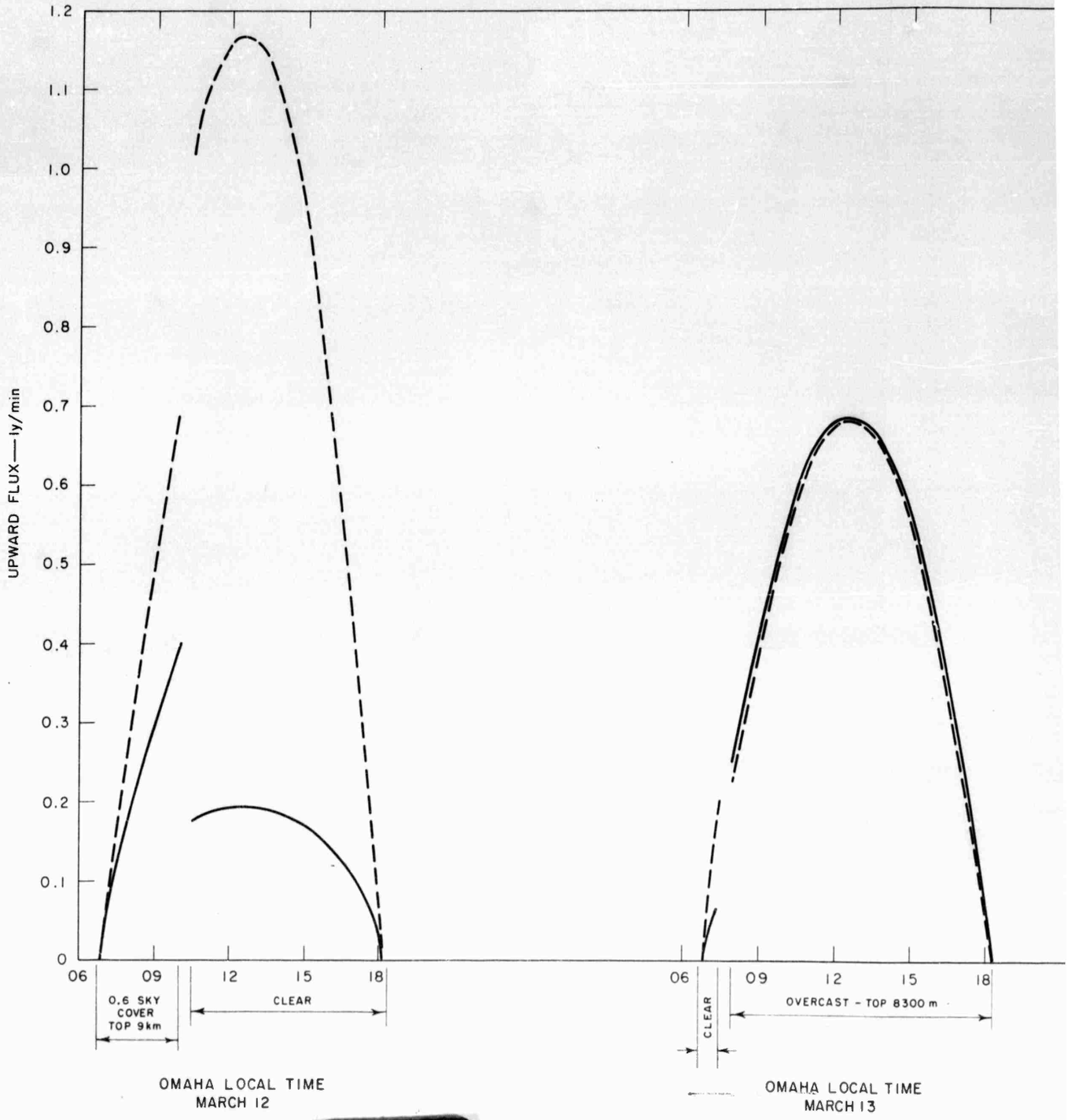

1

UPWARD FLUX OF SOLAR RADIATION FROM THE TOP OF THE
AS A FUNCTION OF LOCAL TIME FOR A

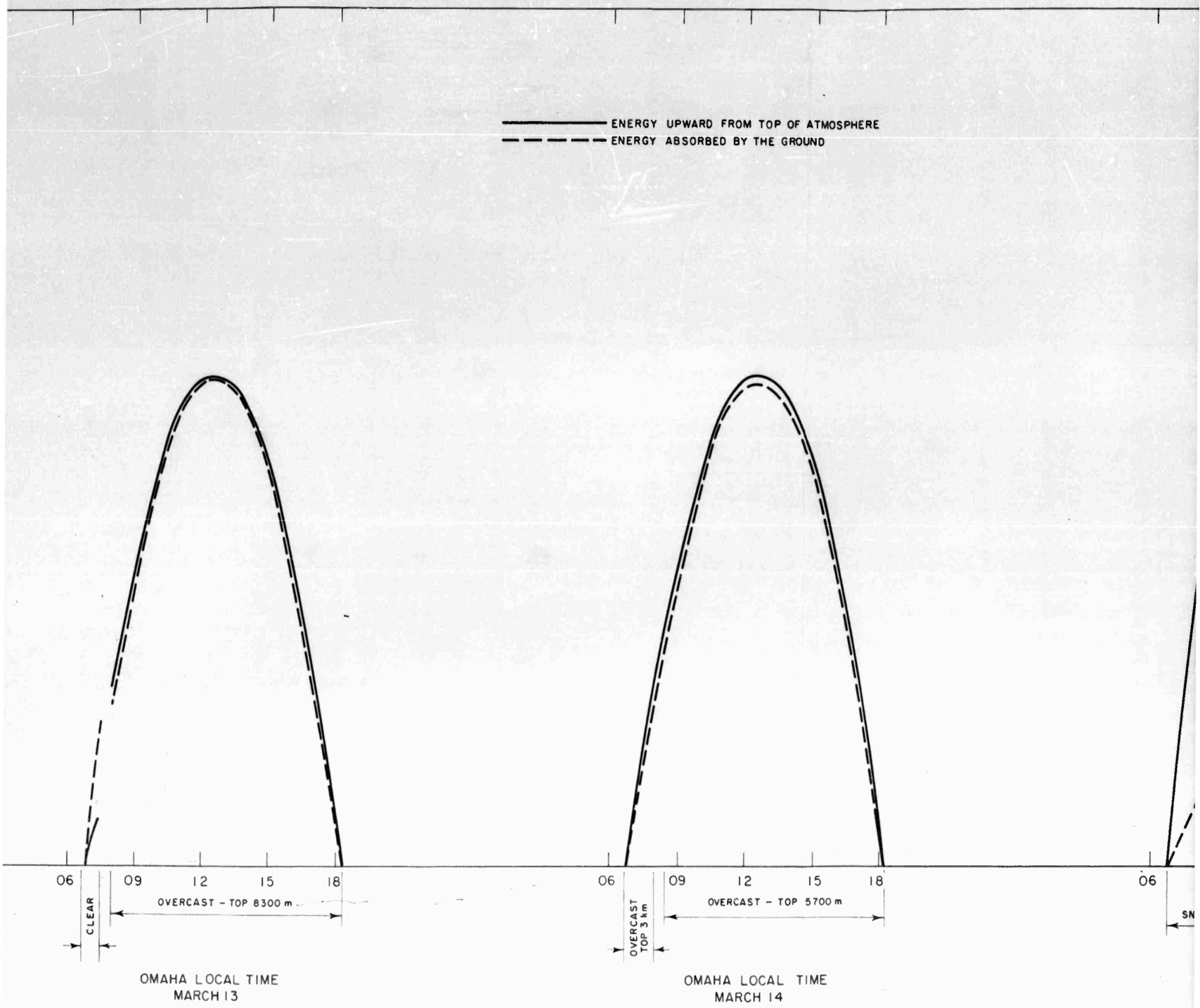

FIG. 16

FLUX OF SOLAR RADIATION FROM THE TOP OF THE ATMOSPHERE AND SOLAR ENERGY ABSORBED BY GROUND AT OMAHA AS A FUNCTION OF LOCAL TIME FOR A SELECTED SYNOPTIC SITUATION IN MARCH 1957

2

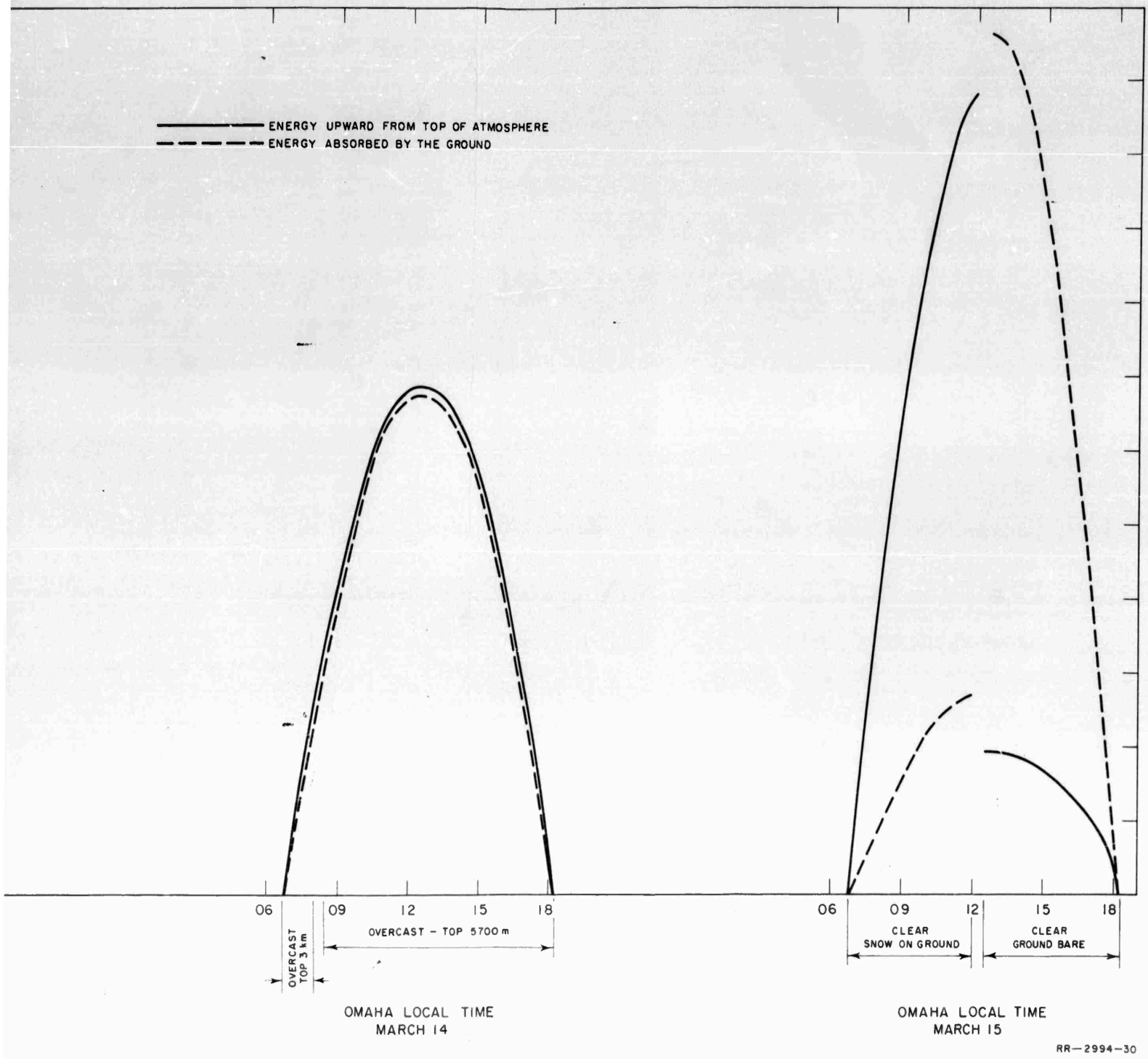

FIG. 16

OF THE ATMOSPHERE AND SOLAR ENERGY ABSORBED BY GROUND AT OMAHA
FOR A SELECTED SYNOPTIC SITUATION IN MARCH 1957

3

$$\log E_v = -0.740 + 0.347 \log V - 0.056 (\log V)^2 - 0.006 (\log V)^3 \quad (6)$$

where V is the precipitable water (cm) in the path of the radiation. If v is the precipitable water in the vertical column, then for the incident parallel solar radiation $V_I = v \sec \theta_o$, and for diffuse radiation, $V_D \approx 1.66$ v.

1. Absorption for Clear-Sky Conditions

If for clear skies, E_{vC} is the energy absorbed from a vertically incident beam per unit time by the water vapor in a vertical air column of a unit cross section, then we can write

$$E_{vC} = E_{IC} + E_{SC} + E_{DC} \quad (7)$$

where E_{IC} is the energy absorbed from the incident parallel sunlight, E_{SC} is that absorbed from the scattered sunlight, and E_{DC} is the energy absorbed from the light diffusely reflected from the underlying surface.

The term E_{IC} generally represents the major component of E_{vC} and is easily computed by Eq. (6) from the data of v and θ_o. For practical purposes, E_{SC} is negligible in comparison to the other terms since water vapor absorbs mainly in the infrared region for which molecular scattering is very small. The term E_{DC} is more important, especially for highly reflecting surfaces. The total water vapor pathlength encountered by the reflected radiation is $V_R = V_I + V_D$, the two terms corresponding to the downward and upward traverses of the atmosphere, respectively. But the absorption in the downward traverse was already accounted for in E_{IC}. Then, for a surface of reflectivity A, we have for the diffusely reflected radiation in a clear atmosphere

$$E_{DC} = A[E(V_R) - E_{IC}] \quad (8)$$

where $E(V_R)$ is evaluated by Eq. (6) for the pathlength V_R. If the change of incident energy with solar angle θ_o is taken into account, the total energy flux absorbed by water vapor in the clear atmosphere is

$$F_C = E_{vC} \cos \theta_o = \{E_{IC} + A[E(V_R) - E_{IC}]\} \cos \theta_o . \quad (9)$$

2. Absorption for Overcast Conditions

The analysis for overcast conditions is complicated by the presence of clouds. A fraction A_T of the incident radiation is reflected (actually back-scattered) from the cloud top, and therefore undergoes two traverses of the water vapor above the cloud. By reasoning similar to that leading to Eq. (9), it is seen that the amount of energy absorbed above the cloud top is

$$E_a = \left\{E_{Ia} + A_T \left[E(V_{Ra}) - E_{Ia}\right]\right\} . \qquad (10)$$

Here V_{Ra} is the total pathlength for the reflected radiation above the cloud top, the downward traverse being for parallel and the upward traverse for diffuse radiation. A small error would be introduced by the actual pathlength being different from V_{Ra} since some of the radiation penetrates a distance into the cloud before being scattered back, and some multiple scattering takes place inside the cloud. Neiburger's measurements indicate that the relatively thin clouds are efficient backscatterers, a cloud of reflectance $A_T = 0.50$ being generally less than 500 feet thick. Since much of the back-scattered radiation would never reach 500 feet into the cloud, 300 feet is perhaps a reasonable average value. The cloud top height would thus be effectively decreased by this amount.

A small part of the fraction $1 - A_T$ which is transmitted through the cloud top is absorbed by the liquid water of the cloud droplets. The effect of this absorption on the water vapor problem is second-order, however, and will be neglected here.

The radiation entering the cloud quickly becomes diffuse, and the effective pathlength for the region below the cloud top is changed thereby from $v_b \sec \theta_o$ to $1.66\ v_b$, where v_b is the precipitable water in vapor form below the cloud top. Multiple scattering by the droplets inside the cloud would increase the mean pathlength somewhat further. Korb, *et al.*,[11] derived a "detour factor" to account for this path extension, the value of which indicates that there may be up to a 50% increase for certain conditions. Smaller increases are more common, however. Their result of the detour factor being less than unity seems of questionable significance,

and they point out that their results represent only order-of-magnitude corrections. Until more advanced methods are available and more information on the cloud characteristics themselves is obtained, it seems premature to introduce a refinement for this pathlength increase by multiple scattering inside the cloud.

For the present computations, it is assumed that the cloud effect for water-vapor absorption, in the region below the cloud top, is a decrease of the downward flux due to the reflectivity A_T of the cloud top, and a change of the effective pathlength by a factor of 1.66 by the radiation becoming diffuse. The total pathlength of the radiation transmitted to the surface is $V_I = v_a \sec \theta_o + 1.66\ v_b$, where v_a is the precipitable water vapor above the cloud top and v_b is that below. The fraction of the incident energy traversing this distance is approximately $1 - A_T$. It is easily seen that the energy absorbed below the cloud top from the downward stream is

$$E_b = (1 - A_T)[E(V_I) - E(V_a)] \ . \tag{11}$$

There will also be some absorption of the surface-reflected radiation. The additional pathlength for this diffuse component is $V \approx 1.66\ v$ and the absorbed energy is

$$E_r = A_T[E(V_r) - E(V_I)] \ . \tag{12}$$

The total energy absorbed by water vapor for the overcast case for solar zenith angle θ_o is then

$$F_0 = (E_a + E_b + E_r) \cos \theta_o \ . \tag{13}$$

The rate of energy absorption by the atmospheric water vapor at Omaha was computed by Eq. (6) for the synoptic case of March 12-15, 1957. Typical results are shown as a function of local time in the diagrams of Fig. 17. The actual radiosonde humidity measurements were used to compute the various pathlengths when such data were available, and at other times humidity data from the vertical time section were used. For periods of partial cloudiness the computations were carried out for both clear and

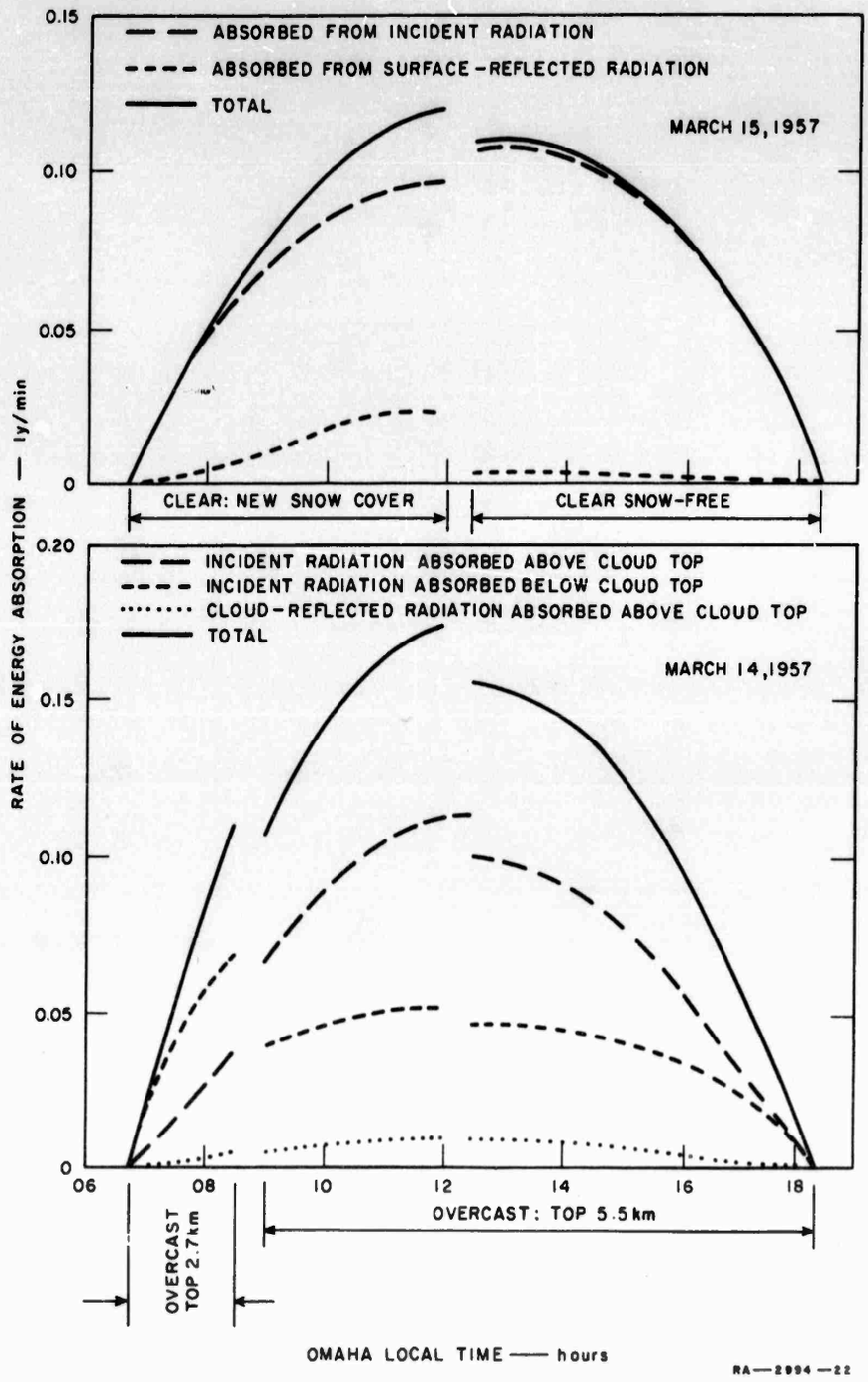

FIG. 17

RATE OF SOLAR ENERGY ABSORPTION BY ATMOSPHERIC WATER VAPOR AT OMAHA AS A FUNCTION OF LOCAL TIME FOR SELECTED SYNOPTIC SITUATION

overcast conditions and the final results were weighted according to the cloud amount. The discontinuities of the curves are the result of assumed discontinuously changed conditions of water-vapor content, cloudiness, or surface reflectivity. The cloud reflectivity was taken as $A_T = 0.50$ for overcast. Surface reflectivity was again assumed to be $A = 0.10$ for the snow-free surface and $A = 0.80$ for new snow.

For clear conditions with snow-free ground (March 15, P.M.) practically all of the absorbed energy is from the downward traverse of the atmosphere, the maximum rate of absorption being of the order 0.13 - 0.15 ly/min. Absorption of surface-reflected radiation contributes only about 1% or 2% for the snow-free case, but strongly reflecting new snow (March 15, A.M.) increases the surface-reflected contribution to a maximum of about 20% of the total. The somewhat greater total absorption which occurred on March 14 is the result of a higher total water-vapor content. A change of cloud-top height from 2.7 km to 5.5 km explains the shift of relative magnitudes of the dashed curves at about 0900 on March 14. The cloud-reflected radiation which is absorbed above the cloud top, represented by the bottom curve of the March 14 diagram, reaches a maximum of about 6% of the total.

Integration of the time rate of energy absorption from sunrise to sunset yields the total energy absorption and percent of extraterrestrial incident flux for each day of the period March 12-15 given in Table I. It is seen that the values agree well with those obtained by other investigators.

TABLE I

TOTAL SOLAR ENERGY AND PERCENT OF EXTRATERRESTRIAL INCIDENT FLUX ABSORBED BY ATMOSPHERIC WATER VAPOR AT OMAHA DURING EACH DAY OF THE PERIOD MARCH 12-15, 1957

Date	Total Absorbed Solar Energy (langleys)	Percent of Extraterrestrial Incident Flux
March 12	66.3	10.8
March 13	65.2	10.6
March 14	77.5	12.6
March 15	56.9	9.3

McDonald[21] used the well-known absorption data of Fowle to obtain an empirical absorptivity a of the form $a(u) = 0.077(u)^{0.30}$ where u(cm) is the total precipitable water vapor in the optical path. Application of this method to the data of March 12 for Omaha yields an absorption value of roughly 20% less than that of Table I. McDonald points out that a question has been raised as to the validity of Fowle's data, and concludes that absolute accuracies of atmospheric water-vapor absorption calculations of not better than 30% are possible at present. In view, however, of the independent absorption measurements of Howard, et al.,[20] which were used by Korb,[11] the 30% maximum accuracy appears pessimistic, but the errors have not been well evaluated as yet in the present study.

D. EFFECTS OF HAZE AND DUST

The radiative effects of haze, dust, and other such particulates in the atmosphere are not well known, partly because of lack of information on the particles themselves and partly because of the difficulties inherent in solving the radiative transfer problem in a turbid atmosphere. Measurements of the physical characteristics of atmospheric suspensoids emphasize their extreme variability of size-frequency distributions and concentrations, both of which are time- and space-dependent. A simple power law is commonly used as the best description of the average size-frequency distribution, while Deirmendjian[22] combined similar laws with an exponential decrease of the concentration with height for computing the intensity distribution in the solar aureole. The measurements further indicate characteristic differences between the aerosols found in continental as opposed to maritime air masses, and urban pollutants are different from those of predominantly rural areas.

The problem of radiative transfer in a turbid medium is receiving considerable emphasis by various authors, but no completely satisfactory solution for the general problem is available as yet. The exact solution of the transfer problem for molecular atmospheres, as obtained originally by Chandrasekhar[9] and further extended by Sekera and collaborators,[10,18] is a major recent development in the field, and it has yielded quantitative data describing completely the radiation field at the upper and lower

boundaries of realistic atmospheric models (Coulson, et al.[23]). Sekera[18] has shown a way of introducing large-particle scattering into the appropriate equations to give a first approximation for the effects of turbidity, and Deirmendjian[22] has used the method for computing the radiative distribution near the forward scattering angles. Fraser[24] has used the Mie-coefficients to compute the normalized scattering matrix for three different models of atmospheric aerosols, thereby providing the possibility of solving the radiative transfer equation for a turbid atmosphere. The numerical solution, however, is still intractable, even for modern computing equipment, because of the complicated dependence of aerosol scattering on scattering angle. The basic Mie theory provides for absorption also, but further computational difficulties arise from its introduction into the system.

For the present problem of determining the radiant energy budget of the selected synoptic situation the measurements by various authors may be used. Most of the work has been for the visible region of the spectrum, but the approximate independence of aerosol scattering with wavelength makes it feasible to use the measurements for the whole solar energy spectrum for a rough evaluation of the energy budget.

Waldram[12] determined the scattering coefficient σ_s and absorption coefficient σ_a for the visible in both clean and industrially polluted atmospheres. The scattering coefficient, given by

$$\sigma_s = -\frac{1}{F}\frac{dF}{dx} \tag{14}$$

where F is flux and x is distance, was obtained by integrating the intensity I_s of the scattered light over the entire solid angle Ω. Thus the energy attenuated from the original incident flux was

$$-dF = \sigma_s F\, dx = \int_\Omega I_s\, d\omega . \tag{15}$$

Values of σ_s varied from 8.0×10^{-6}/ft for very clean air to 2.5×10^{-3}/ft for foggy conditions of 1000 yards visual range. In moderate visibilities

(about 6 miles) $\sigma_s \approx 1.6 \times 10^{-4}$/ft. Considerable variation with height was found to exist through the entire layer 0 to 30,000 feet altitude. In clean atmospheres there was generally, but not always, a decrease of σ_s with height of an amount roughly proportional to the decrease of pure air scattering with height. For polluted atmospheres large fluctuations occurred, particularly in the lower atmospheric layers.

The shape of the polar scatter diagram is of obvious importance in energy budget studies. For primary molecular scattering, the scattered energy is directed equally into the upward and downward hemispheres, regardless of sun elevation. Multiple molecular scattering changes the partition a small amount by increasing the backscatter to somewhat more than half the total (Coulson[13]). The predominantly forward scattering of aerosol particles, however, alters this simple pattern, making the downward component larger in general, and introducing a solar angle dependence. Only for the sun at the horizon would the upward- and downward-scattered components be equal. Various empirically derived curves have been fitted to the measured polar intensity distributions, but they are of dubious value because of the great variability of the natural aerosol properties and the difficulty of measuring accurately the intensity near the forward direction. The more fundamental approach, employed by Fraser,[24] of comparing the measured polar distribution with that computed for representative aerosol models of known characteristics holds great promise, but further work is required. For instance, Fraser found wide discrepancies between his computed distributions and Waldram's measurements. He suggested an aerosol model with a larger number of particles with high refractive index, but apparently such a model has not been investigated.

From measurements of total transmission, T, and the scatter coefficient, σ_s, it is possible to compute the absorption coefficient, σ_a, from the relation

$$\sigma_a = \frac{\sigma_s x - \ln T}{x} \tag{16}$$

where $\underline{x}$ is distance through the medium. Waldram concluded from his measurements that the "phenomena of absorption and scatter appear to be

independent." It is known from theory that, for a single particle at least, the two are not independent, but apparently the effects of interdependence tended to be small for the conditions prevailing at the time of Waldram's measurements. Generally the absorption was found to be appreciable only when smoke was present, at which time σ_a was usually in the range $1.0 \times 10^{-4}/\text{ft} \leq \sigma_a \lesssim 4.0 \times 10^{-4}/\text{ft}$ and was confined to more or less distinct layers of a few hundred feet thickness. In smoke-free conditions σ_a was of the order of $10^{-5}/\text{ft}$, and in a case of heavy pollution it reached $6 \times 10^{-4}/\text{ft}$.

For a rough evaluation of the effect of scattering and absorption in the March situation at Omaha, a three-layer model of the atmosphere was constructed and the parameters of each layer were estimated from Waldram's measurements. The model is shown schematically in Fig. 18. The bottom layer, 2000 feet in thickness, is assumed to have variable scattering and absorption coefficients, the values depending on the amount of industrial pollution present. Low visibilities at Omaha on March 13 indicate the presence of industrial pollution, while very clear air on March 15, following the frontal passage, shows no such pollution. The coefficients were assumed to change accordingly, the assumed values being $\sigma_s = 7.5 \times 10^{-5}/\text{ft}$, $\sigma_a = 1.0 \times 10^{-4}/\text{ft}$ for polluted air and $\sigma_s = 1.0 \times 10^{-5}/\text{ft}$, $\sigma_a = 0$ for clear air. (The effects of haze and dust are not computed for cloudy periods, as their effects are probably small compared to those of clouds.) The assumption of negligible absorption in the absence of industrial pollution is substantiated by both the measurements of Waldram and an equivalent statement by Van de Hulst.[25] The layer between 2000 and 30,000 feet altitude is assumed to have no absorption and an average scattering coefficient, derived from Waldram's measurements for clear air, of $\sigma_s = 1 \times 10^{-5}/\text{ft}$. Above 30,000 feet Rayleigh scattering is assumed, an optical thickness of $\tau = 0.04$ being reasonable for the entire mass of air above that level. Optical thicknesses due to scattering in the first and second layers were computed by the definition

$$\tau_s(z) = \int_{z_i}^{z_j} \sigma_s \, dz$$

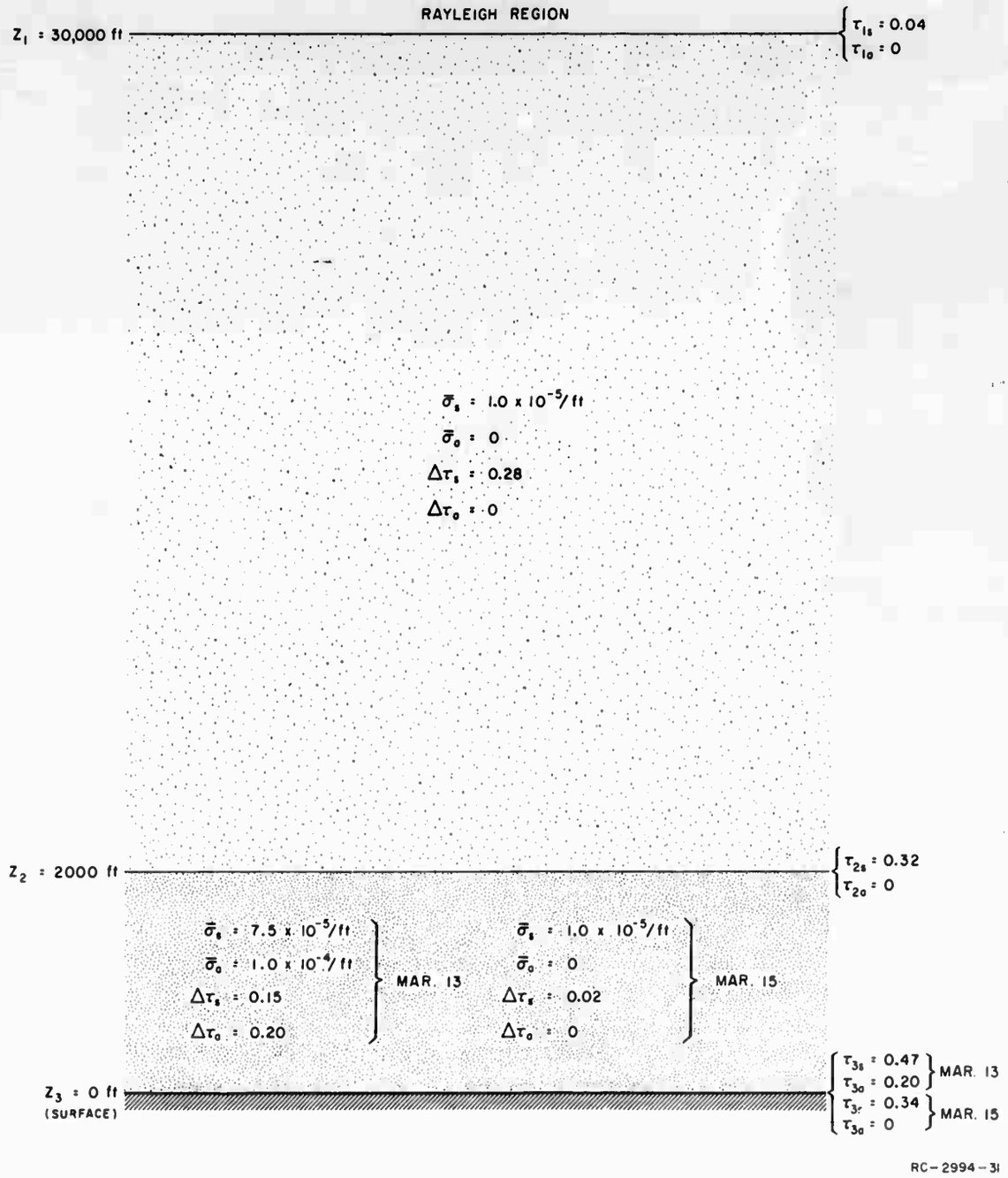

FIG. 18

SCHEMATIC DIAGRAM OF THREE-LAYER ATMOSPHERIC MODEL
Adapted from Waldram's measurements

and similarly for the absorption optical thickness, τ_a. Finally, the attenuation of the incident parallel beam, inclined at angle $\theta_o = \arccos \mu_o$ from the vertical, by scattering in the entire atmosphere is

$$1 - e^{-\tau_s/\mu_o}$$

For convenience of computation it was assumed that the absorption and scattering are independent processes and that the absorption occurs from the final surface radiation field existing after scattering (i.e., scattering occurs first). Thus it is reasonable to consider all of the radiation as being diffuse for the absorption process, and that the effective absorption optical thickness is thereby 1.66 τ_a, independent of solar angle. It is readily seen that the following relations exist among the transmissivity T, absorptivity a, and backscatter b for the total atmospheric model:

$$\begin{aligned} 1 &= T + a + b \\ T &= e^{-1.66\tau_a} \left[e^{-\tau_s/\mu_o} + f(1 - e^{-\tau_s/\mu_o})\right] \\ a &= (1 - e^{-1.66\tau_a})\left[e^{-\tau_s/\mu_o} + f(1 - e^{-\tau_s/\mu_o})\right] \\ b &\doteq (1 - f)(1 - e^{-\tau_s/\mu_o}) \ . \end{aligned} \tag{17}$$

Here f is the fraction of the scattered energy which is directed into the downward hemisphere.

To estimate the portion of the energy which is backscattered and lost to the system it is necessary to integrate the appropriate intensity phase function over the upward and downward hemispheres. Plaskovskaia-Fesenkova[26] describes the scattering diagram for clear air by the empirically derived function

$$P(\psi) = 1 + 0.49 \cos \psi + 1.093 \cos^2 \psi + 0.704 \cos^3 \psi \tag{18}$$

where ψ is the scattering angle measured from the forward direction. The forward component of the scattered energy is, except for a constant, given by

$$\int_{0}^{\pi/2} P(\psi) \cos \psi \sin \psi \, d\psi \tag{19}$$

and the backward component by

$$\int_{\pi/2}^{\pi} P(\psi) \cos \psi \sin \psi \, d\psi \tag{20}$$

On carrying out the integrations and taking the ratio of the components, we find the forward component to be 1.51 times the backward component.

Gibbons[27] describes the scattering diagram for a clear atmosphere by the empirically derived function

$$G_1(\psi) = 1 + \cos^{16} \frac{\psi}{2} . \tag{21}$$

For this the forward component is 1.36 times the backward component.

These values would be the ratio of downward to upward energy in the atmosphere only for vertical incidence. Obviously for horizontal incidence the ratio would be 1.0, and an effective value applicable for the whole day would be somewhere between the two limiting cases. For present purposes a value of 1.2 is taken as a reasonable ratio for the clear atmosphere.

For a noticeably hazy atmosphere Gibbons[27] fitted the observed intensity distributions adequately by the relation

$$G_2(\psi) = 1 + 9 \cos^{16} \frac{\psi}{2} . \tag{22}$$

Substitutions of this in Eq. (19) and Eq. (20) yields a ratio of forward-to-backward-scattered energy of 4.20, applicable for vertical incidence. On considering the change with sun elevation, a ratio of 2.0 seems reasonable for the effective mean value for the polluted atmosphere at Omaha. This predominantly forward scattering, however, prevailed in only the lower 2,000 feet, which contains only about 8% of the total atmosphere, so the mean scattering pattern would not be changed greatly from the clear

case. A ratio of forward-to-backward-scattered energy of 1.5 seems reasonable for the total atmosphere with the presence of the low-level pollution.

The fractional distribution of the extraterrestrial solar flux computed for the above model is shown in Fig. 19 as a function of local time, for the clear atmosphere of March 15 (solid curves) and the industrially polluted atmosphere of March 13 (dashed curves). The existence of a 2,000-foot pollution layer had little effect on the total backscattering characteristics. The effect of the larger scattering coefficient for the polluted case was offset by the predominantly forward

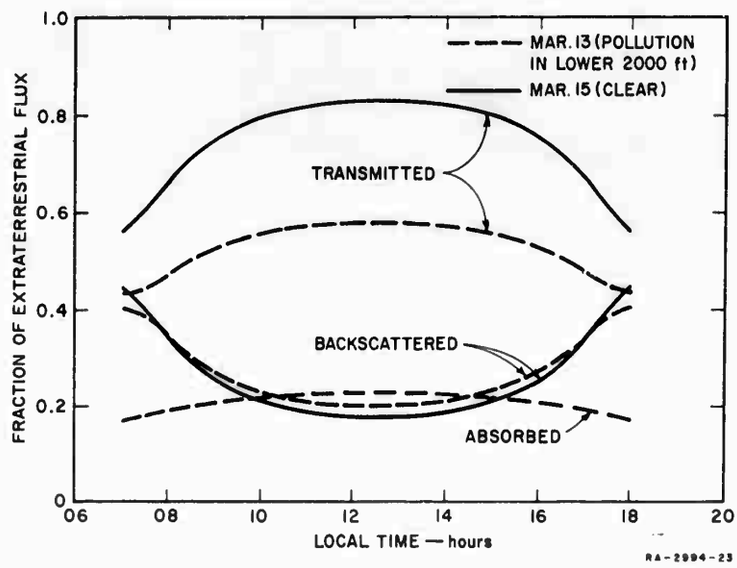

FIG. 19

FRACTIONAL DISTRIBUTION OF EXTRATERRESTRIAL INCIDENT ENERGY AT OMAHA AS A FUNCTION OF LOCAL TIME, FOR CLEAR AND INDUSTRIALLY POLLUTED ATMOSPHERIC CONDITIONS

scattering by aerosols. Evidently, the ratio of the diffusely transmitted to the directly transmitted radiation would be increased by the pollutants. Absorption in the 2,000-foot polluted layer is a major factor in the polluted atmosphere, being greater than the total backscattering during part of the sunlit period. The actual absorption may have been even larger, as the assumption of independent and consecutive scattering and

absorption tends to minimize absorption. The fraction transmitted is seen to be always less than 85%, even for the clear atmosphere.

Figure 20 is a plot of the energy involved in the various processes, as a function of local time. The solar constant was taken as 2.0 ly/min. The amount of energy backscattered to space is relatively insensitive to solar position except at large solar zenith angles, whereas there is a strong diurnal variation of the other components.

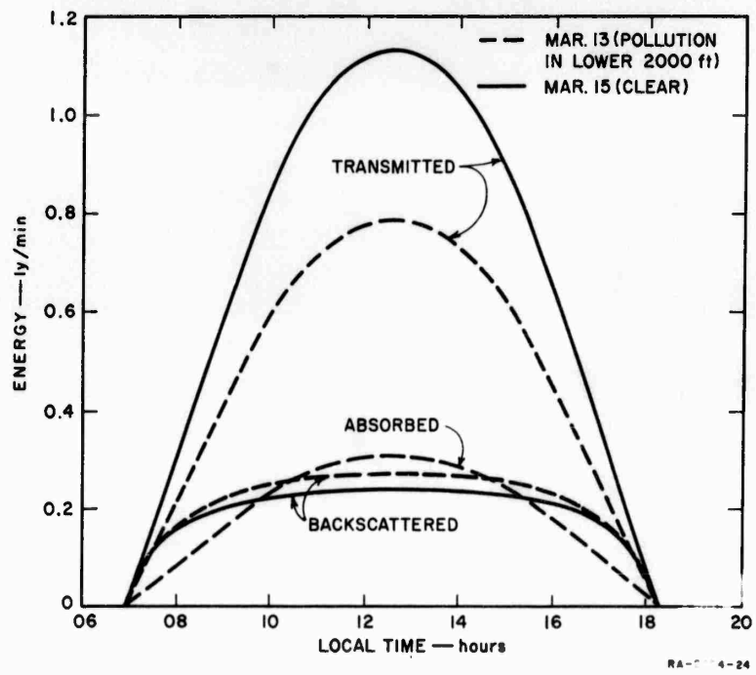

FIG. 20

DISTRIBUTION OF INCIDENT SOLAR ENERGY AT OMAHA AS A FUNCTION OF LOCAL TIME, FOR CLEAR AND INDUSTRIALLY POLLUTED ATMOSPHERIC CONDITIONS
The Solar Constant was Taken as 2.0 ly/min.

Integration under the curves of Fig. 20 yields the daily energy distribution given in Table II for the various processes. The values compare well with the measurements available in similar conditions. From an extensive study of daylight illumination for photographic exposure, Jones and Condit[28] found that light haze decreases the illuminance on a horizontal surface at the ground by 27% from its value for clear conditions.

TABLE II

SOLAR ENERGY DISTRIBUTION BY ATMOSPHERIC PROCESSES FOR THE ENTIRE DAY FOR DIFFERENT ATMOSPHERIC CONDITIONS AT OMAHA

Atmospheric Characteristics	Process	Energy (langleys)	Percent of Incident Extraterrestrial Flux
Industrial pollution in lower 2000 feet, clear above.	Backscatter	146.3	23.8
	Absorption	131.8	21.5
	Transmission	335.9	54.7
Clear	Backscatter	133.1	21.7
	Absorption	0	0
	Transmission	480.9	78.3

The analogous decrease here is 30%. Another comparison can be made by combining the computed Rayleigh backscatter, given previously in Fig. 10, with the dust attenuation factor of Houghton,[29] namely, $1-(0.95)^m$ where $\underline{m}$ is the air mass. Houghton estimated that 1/2 of the depleted energy was absorbed, 1/4 backscattered to space and 1/4 diffusely transmitted. These effects are shown by the curves of Fig. 21, Curve (a) being for dust and (b) for Rayleigh scattering for the spectral region $3100\ \text{Å} \leq \lambda \leq 25{,}000\ \text{Å}$. Curve (c), the sum of (a) and (b), represents the total backscatter by the clear atmosphere. This should be compared with Curve (e), which was transferred directly from Fig. 19. It is seen that only about half of the backscatter computed from Waldram's measurements is accounted for. In an effort to obtain better agreement, it was thought that Rayleigh scattering should be represented by that for only the visible, since Waldram's measurements were for visible light. Curve (d) is the sum of the fractional Rayleigh backscatter for $4000\ \text{Å} \leq \lambda \leq 7000\ \text{Å}$ and the dust backscatter of Curve (a). There is still considerable discrepancy between Curves (d) and (e), indicating that the effects of dust are not adequately represented for this case by Houghton's simple law.

Blackwell, et al.[30]* determined the amount of absorption and scattering by atmospheric particulates in the clear atmosphere at Kew Observatory as

* Results quoted by Sheppard[31] are given here, as the original paper was not available.

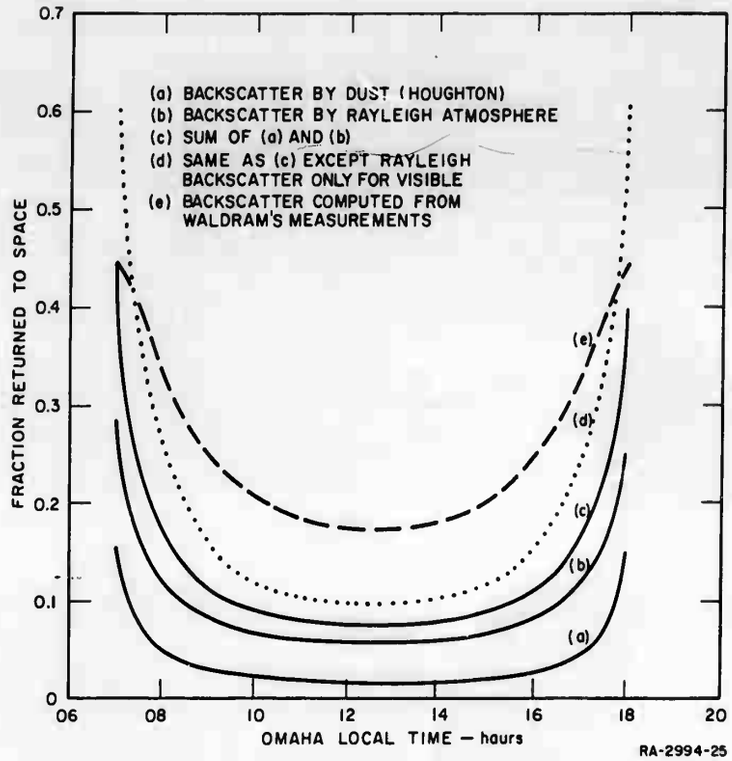

FIG. 21

FRACTION OF INCIDENT ENERGY BACKSCATTERED TO SPACE BY CLEAR ATMOSPHERE

given in Table III. It should be noted that this is in addition to Rayleigh scattering. If these values are added to the Rayleigh effect, given by Curve (c) of Fig. 21, reasonably good agreement with the results derived from Waldram's measurements, Curve (e), is obtained.

TABLE III

FRACTIONS OF EXTRATERRESTRIAL VERTICAL SOLAR ENERGY FLUX ABSORBED AND BACKSCATTERED BY ATMOSPHERIC PARTICULATES AT KEW

Solar Zenith Angle	36°	53°	66°	78°
Fraction absorbed	0.06	0.08	0.11	0.16
Fraction backscattered to space	0.05	0.05	0.04	0.02

Source: Blackwell, et. al. (Ref. 30).

E. OZONE ABSORPTION OF SOLAR RADIATION

A large number of investigations of the atmospheric ozone problem have established the main features of the space and time distribution of ozone and its role in the atmospheric heat balance. The excellent monograph by Craig[32] outlines the history of ozone work and includes a relatively complete bibliography of the field up to 1950. The main developments since that time have been (1) a re-determination of the absorption coefficients (Vigroux[33]), (2) further measurements of the amount and distribution of atmospheric ozone as a function of height, geographical location, season, and weather situation (Dütsch,[34] Ramanathan and Kulkarni,[35] Ramanathan and Dave[36]), (3) more accurate data on the ultraviolet solar spectrum (Johnson[37]), and (4) new computations of atmospheric temperature changes in the ozonosphere (Murgatroyd and Goody,[38] Pressman[39]).

In order to compute the amount of energy absorbed by ozone at Omaha during the selected synoptic situation, use was made of the 3-year series of umkehr measurements at Arosa reported by Dütsch.[34] The mean ozone distribution for March was used as being representative of conditions at Omaha for the entire four-day period March 12-15, up to the limit of Dütsch's data at 47.8 kilometers. An exponential decrease of ozone content with height was assumed from 47.8 km to 70 km, the value at 70 km being that given by Johnson.[37] The ozone amount above 70 km was assumed negligible. Figure 22 shows the vertical distributions for Arosa and White Sands, New Mexico, together with the extrapolation assumed for Omaha. The total ozone amount between 10 and 70 kilometers was 0.33 cm at NTP.

The method of Craig[40] was used for computing the ozone absorption of solar radiation for the sunrise-to-sunset period at Omaha. Use of the more recent absorption coefficients obtained by Vigroux[33] would change the absolute values somewhat, but not the general patterns of ozone absorption. The total energy E_z absorbed per unit volume at altitude z is given by

$$E_z = n \int_0^\infty I_{o\lambda} \alpha_\lambda e^{-\alpha_\lambda N} d\lambda \qquad (23)$$

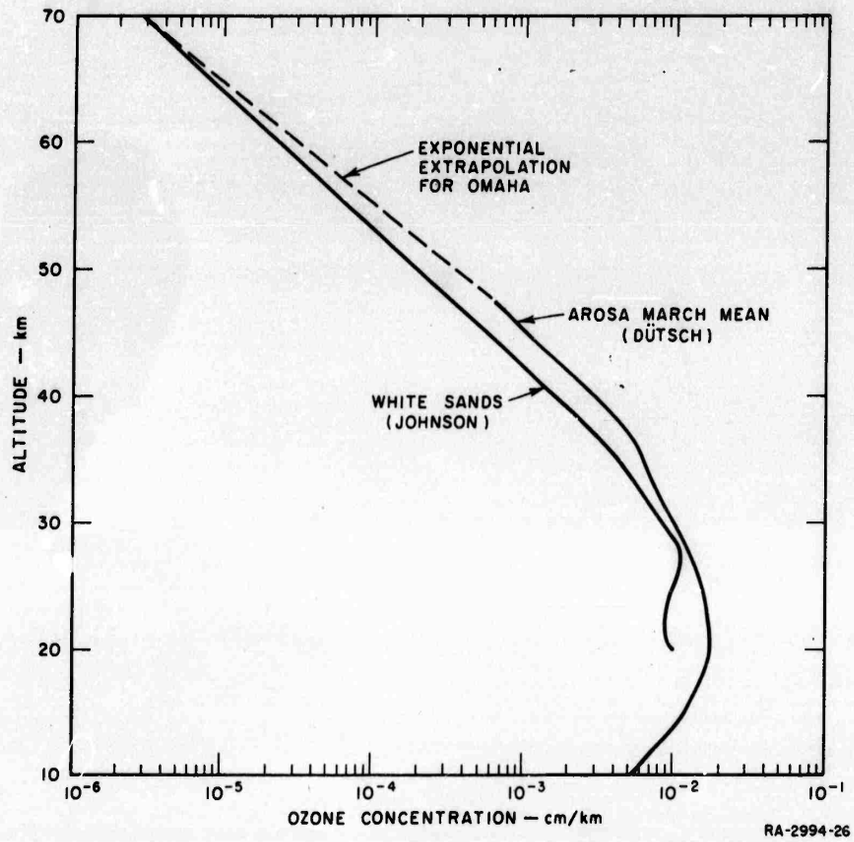

FIG. 22

MEASURED VERTICAL DISTRIBUTIONS OF OZONE (SOLID CURVE) AT AROSA AND WHITE SANDS, AND EXPONENTIAL EXTRAPOLATION (DASHED CURVE) ASSUMED FOR OMAHA

where $\underline{n}$ is the amount of ozone per unit volume, $I_{o\lambda}$ the monochromatic intensity at level $\underline{z}$, and α_λ the monochromatic ozone absorption coefficient. The ozone pathlength N is given by the relation

$$N = \int_z^\infty n \sec \theta_o \, dz \tag{24}$$

for the incident parallel solar radiation. Effects of atmospheric scattering are neglected here. The rate of temperature change by ozone absorption is

$$\frac{\partial T}{\partial t} = \frac{E_z}{\rho_z c_p} \tag{25}$$

ρ_z being the air density at level $\underline{z}$, and c_p the specific heat of air at constant pressure.

Curves of the heating rate by ozone absorption of solar radiation as a function of height are shown in Fig. 23 for different zenith angles of the sun. At the highest levels the heating rate is essentially independent of solar position and amounts to a few tenths of a degree per hour.

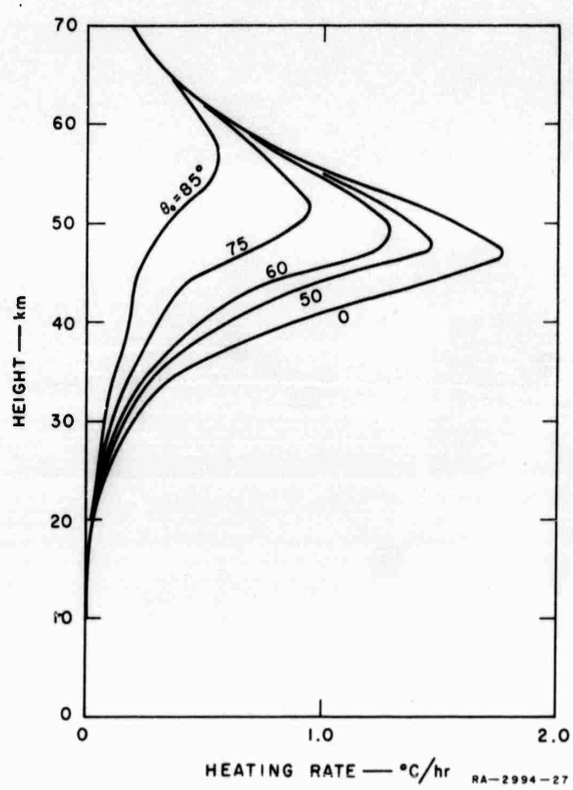

FIG. 23

RATE OF HEATING BY OZONE ABSORPTION OF SOLAR RADIATION AS A FUNCTION OF HEIGHT FOR DIFFERENT SOLAR ZENITH ANGLES

The maximum rate is seen to be 1.7°C/hr for zenith sun. The noon solar zenith angle in March at Omaha is about 47°, for which the maximum heating rate of 1.5°C/hr occurs at 47 km.

A time integration of the heating rate for the sunrise-to-sunset period at Omaha results in the diurnal temperature increase by ozone

absorption as a function of height given in Fig. 24. The 12.5°C maximum is considerably greater than the 8°C maximum given by Murgatroyd and Goody,[38] reflecting the greater total ozone content assumed here. The 50 km height of the maximum agrees well with their results, and with the well known temperature maximum in that region.

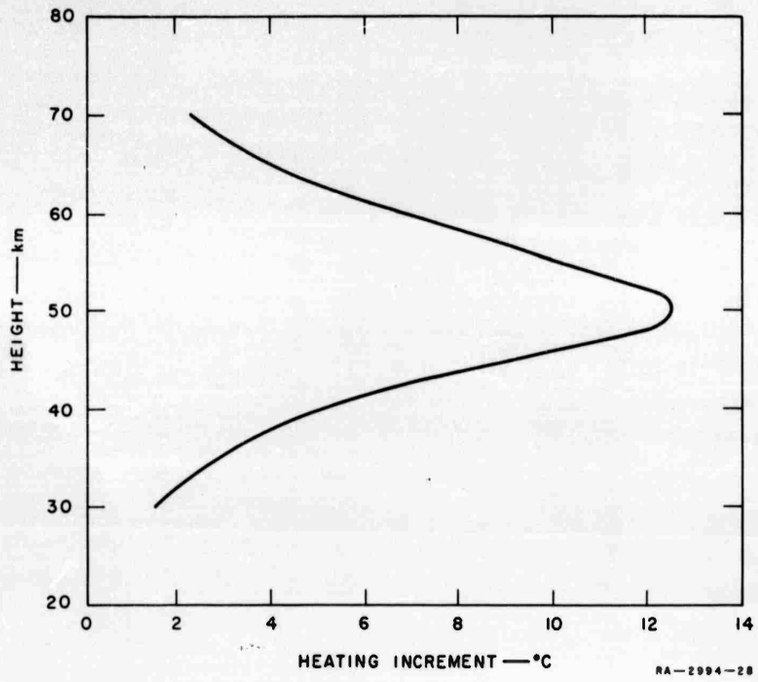

FIG. 24

DIURNAL TEMPERATURE INCREASE BY OZONE ABSORPTION OF SOLAR RADIATION AT OMAHA IN MARCH 1957, AS A FUNCTION OF HEIGHT

The rate of energy absorption by the total ozone content of the atmosphere at Omaha for March 15 is shown as a function of local time by the curve of Fig. 25. The maximum of 0.285 ly/min occurring at noon represents 2.1% of the extraterrestrial incident energy. Integration over the sunlit period shows a total absorption by ozone of 13.55 ly, which is 2.2% of the total incident solar energy for the period.

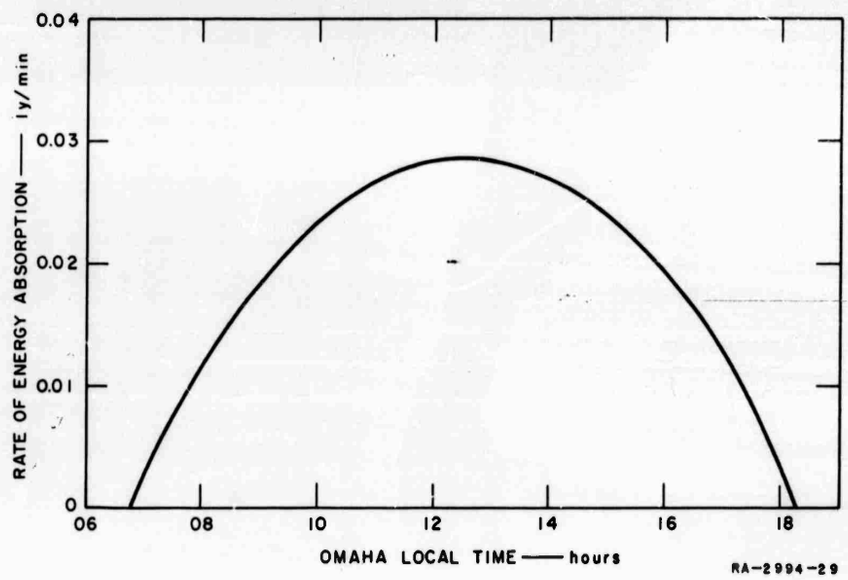

FIG. 25

RATE OF SOLAR ENERGY ABSORPTION BY OZONE AT OMAHA
IN MARCH 1957, AS A FUNCTION OF LOCAL TIME

ACKNOWLEDGMENT

The valuable discussions and suggestions of Profs. Zdenek Sekera and Yale Mintz, who visited the project as consultants and of Dr. Manfred M. Holl, project leader, are gratefully acknowledged. Likewise, appreciation is expressed to Mr. Harmon Wildermuth for his assistance in the long-wave calculations.

APPENDIX

THE MONOCHROMATIC REFLECTANCE R_ν OF THE ATMOSPHERE-SURFACE SYSTEM FOR VARIOUS VALUES OF THE OPTICAL THICKNESS τ AND SURFACE REFLECTIVITY, A

Appendix

THE MONOCHROMATIC REFLECTANCE R_ν OF THE ATMOSPHERE-SURFACE SYSTEM FOR VARIOUS VALUES OF THE OPTICAL THICKNESS τ AND SURFACE REFLECTIVITY, A

τ	λ(Å)	μ_o	Surface Reflectivity, A						
			0	0.05	0.10	0.15	0.25	0.50	0.80
1.0	3120	0.02	0.751	0.758	0.765	0.773	0.790	0.840	0.922
		0.10	0.704	0.712	0.721	0.730	0.750	0.809	0.908
		0.20	0.650	0.660	0.670	0.681	0.705	0.775	0.891
		0.40	0.546	0.558	0.572	0.586	0.616	0.707	0.859
		0.60	0.458	0.474	0.490	0.507	0.543	0.651	0.831
		0.80	0.392	0.409	0.427	0.446	0.486	0.608	0.811
		0.92	0.359	0.377	0.396	0.416	0.469	0.587	0.801
		1.00	0.340	0.359	0.378	0.399	0.443	0.575	0.795
0.50	3660	0.02	0.675	0.687	0.698	0.711	0.737	0.809	0.915
		0.10	0.610	0.624	0.638	0.653	0.684	0.771	0.898
		0.20	0.523	0.540	0.558	0.576	0.614	0.720	0.875
		0.40	0.383	0.405	0.428	0.451	0.500	0.638	0.838
		0.60	0.297	0.322	0.348	0.374	0.430	0.587	0.816
		0.80	0.241	0.268	0.296	0.325	0.385	0.554	0.801
		0.92	0.216	0.244	0.273	0.303	0.365	0.540	0.795
		1.00	0.202	0.231	0.260	0.291	0.354	0.532	0.791
0.25	4365	0.02	0.609	0.625	0.641	0.658	0.693	0.785	0.909
		0.10	0.503	0.524	0.545	0.566	0.610	0.727	0.884
		0.20	0.375	0.401	0.427	0.454	0.509	0.657	0.854
		0.40	0.238	0.270	0.302	0.335	0.402	0.582	0.822
		0.60	0.173	0.207	0.242	0.278	0.351	0.546	0.807
		0.80	0.136	0.172	0.208	0.245	0.321	0.525	0.798
		0.92	0.120	0.157	0.194	0.231	0.309	0.517	0.794
		1.00	0.112	0.148	0.186	0.224	0.302	0.512	0.792
0.15	4950	0.02	0.569	0.588	0.607	0.627	0.667	0.771	0.905
		0.10	0.406	0.432	0.459	0.486	0.541	0.684	0.869
		0.20	0.270	0.302	0.335	0.368	0.436	0.612	0.839
		0.40	0.158	0.195	0.233	0.271	0.349	0.552	0.814
		0.60	0.111	0.151	0.191	0.231	0.313	0.528	0.803
		0.80	0.086	0.126	0.167	0.209	0.293	0.514	0.798
		0.92	0.076	0.116	0.158	0.200	0.285	0.508	0.796
		1.00	0.070	0.111	0.153	0.195	0.281	0.505	0.794

Note: The solar zenith angle θ_o is given in terms $\mu_o = \cos \theta_o$.

Appendix (Continued)

τ	λ(Å)	μ_o	Surface Reflectivity, A						
			0	0.05	0.10	0.15	0.25	0.50	0.80
0.10	5410	0.02	0.541	0.562	0.583	0.605	0.648	0.760	0.902
		0.10	0.323	0.355	0.386	0.418	0.482	0.647	0.855
		0.20	0.199	0.236	0.273	0.310	0.386	0.582	0.828
		0.40	0.111	0.152	0.193	0.235	0.319	0.536	0.809
		0.60	0.077	0.119	0.162	0.205	0.293	0.518	0.802
		0.80	0.059	0.102	0.146	0.190	0.279	0.509	0.798
		0.92	0.052	0.095	0.139	0.183	0.273	0.505	0.797
		1.00	0.048	0.091	0.136	0.180	0.270	0.503	0.796
0.05	6440	0.02	0.475	0.352	0.385	0.419	0.486	0.656	0.862
		0.10	0.198	0.136	0.180	0.225	0.315	0.541	0.815
		0.20	0.111	0.094	0.141	0.188	0.282	0.519	0.807
		0.40	0.059	0.072	0.120	0.168	0.265	0.508	0.802
		0.60	0.040	0.065	0.113	0.162	0.259	0.504	0.800
		0.80	0.030	0.061	0.110	0.158	0.256	0.501	0.799
		0.92	0.026	0.059	0.108	0.157	0.255	0.501	0.799
		1.00	0.024	0.059	0.107	0.156	0.254	0.500	0.799
0.02	8090	0.02	0.319	0.352	0.385	0.419	0.486	0.656	0.862
		0.10	0.091	0.136	0.180	0.225	0.315	0.541	0.815
		0.20	0.048	0.094	0.141	0.188	0.282	0.519	0.807
		0.40	0.024	0.072	0.120	0.168	0.265	0.508	0.802
		0.60	0.016	0.065	0.113	0.162	0.259	0.504	0.800
		0.80	0.012	0.061	0.110	0.158	0.256	0.501	0.799
		0.92	0.011	0.059	0.108	0.157	0.255	0.501	0.799
		1.00	0.011	0.059	0.107	0.156	0.254	0.500	0.799
0.01	9600	0.02	0.197	0.237	0.277	0.317	0.396	0.597	0.838
		0.10	0.048	0.095	0.142	0.189	0.284	0.521	0.808
		0.20	0.024	0.073	0.121	0.170	0.267	0.510	0.803
		0.40	0.012	0.061	0.110	0.159	0.257	0.504	0.801
		0.60	0.008	0.057	0.107	0.156	0.254	0.502	0.800
		0.80	0.006	0.055	0.105	0.154	0.253	0.501	0.800
		0.92	0.005	0.055	0.104	0.153	0.252	0.500	0.800
		1.00	0.005	0.054	0.104	0.153	0.252	0.500	0.799
0.003	12960	0.02	0.068	0.115	0.161	0.208	0.301	0.534	0.813
		0.10	0.013	0.063	0.112	0.161	0.260	0.506	0.802
		0.20	0.006	0.056	0.105	0.155	0.254	0.502	0.801
		0.40	0.002	0.052	0.102	0.152	0.251	0.500	0.800
		0.60	0.001	0.051	0.101	0.151	0.250	0.500	0.800
		0.80	0.001	0.050	0.100	0.150	0.250	0.500	0.800
		0.92	0.000	0.050	0.100	0.150	0.250	0.500	0.800
		1.00	0.000	0.050	0.100	0.150	0.250	0.500	0.800

Appendix (Concluded)

τ	λ(Å)	μ_o	Surface Reflectivity, A						
			0	0.05	0.10	0.15	0.25	0.50	0.80
0.001	17000	0.02	0.023	0.072	0.121	0.170	0.267	0.512	0.805
		0.10	0.004	0.054	0.104	0.153	0.253	0.502	0.801
		0.20	0.002	0.051	0.101	0.151	0.251	0.501	0.800
		0.40	0.000	0.050	0.100	0.150	0.250	0.500	0.800
		0.60	0.000	0.050	0.100	0.150	0.250	0.500	0.800
		0.80	0.000	0.050	0.100	0.150	0.250	0.500	0.800
		0.92	0.000	0.050	0.100	0.150	0.250	0.500	0.800
		1.00	0.000	0.050	0.100	0.150	0.250	0.500	0.800

REFERENCES

1. J. London, "A Study of the Atmospheric Heat Balance," Final Report, Contract AF 19(122)-165, New York University, New York City (1957).
2. J. E. Wilk, "Evaluation of the AN/APQ-39(XA-3) Cloud Detector Radar," Final Report, Contract AF 19(604)-1395, University of Illinois, Urbana, Illinois (1958).
3. W. M. Elsasser, "Heat Transfer by Infrared Radiation in the Atmosphere," Harvard Meteorological Studies, 6, Harvard University, Blue Hill Meteorological Observatory, Milton, Mass. (1942).
4. J. V. Hales and W. G. Zdunkowski, "The Long Wave Flux Density Leaving the Earth under Various Meteorological Conditions," Scientific Report 1, Contract AF 19(604)-2418, Intermountain Weather, Inc., Salt Lake City, Utah (1959).
5. J. E. Alder, "The Distribution of Water Vapor Radiative Cooling in Outbreak of Polar Air," Quarterly Progress Report 5, Contract AF 19(122)-256, Department of Meteorology, University of Utah, Salt Lake City, Utah (1951).
6. T. E. Hoffer, "A Study of the Long Wave Radiation Balance in Certain Typical Air Masses," Quarterly Progress Report 5, Contract AF 19(122)-256, Department of Meteorology, University of Utah, Salt Lake City, Utah (1951).
7. R. Geiger, The Climate Near the Ground, (Harvard University Press, Cambridge, Mass., 1950).
8. H. H. Lettau and B. Davidson, Exploring the Atmosphere's First Mile (Pergamon Press, Inc., New York City, 1957).
9. S. Chandrasekhar, Radiative Transfer (Clarendon Press, Oxford, 1950).
10. Z. Sekera and Collaborators, "Investigation of Polarization of Sky-light," Final Report, Contract AF 19(122)-239, Department of Meteorology, University of California, Los Angeles (1955).
11. G. Korb, J. Michalowsky, and F. Möller, "Investigations on the Heat Balance of the Troposphere," Tech. Report 1, Contract AF 61(514)-863, J. Gutenberg University, Mainz, Germany (1956); also Tech. Report 2 (1957).
12. J. M. Waldram, "Measurement of the Photometric Properties of the Upper Atmosphere," Trans. Illum. Eng. Soc. (London) 10, pp. 147-187 (1945).
13. K. L. Coulson, "Characteristics of the Radiation Emerging from the Top of a Rayleigh Atmosphere - Part I: Intensity and Polarization," J. of Planet. Space Soc. 1, pp. 265-276; also "Part II: Total Upward Flux and Albedo," pp. 277-284 (1959).

14. Z. Sekera and G. Blanch, "Tables Relating to Rayleigh Scattering of Light in the Atmosphere," Scientific Report 3, Contract AF 19(122)-239, Department of Meteorology, University of California, Los Angeles (1952).

15. Z. Sekera and E. V. Ashburn, "Tables Relating to Rayleigh Scattering of Light in the Atmosphere," NAVORD Report 2061, U.S. Naval Ordnance Test Station, China Lake, Calif. (1953).

16. S. Chandrasekhar and D. D. Elbert, "The Illumination and Polarization of the Sunlit Sky on Rayleigh Scattering," Trans. Am. Phil. Soc., New Series 44, Part 6, pp. 643-728 (1954).

17. D. Deirmendjian, "Attenuation of Light in the Earth's Atmosphere and Related Problems," Scientific Report 1, Contract AF 19(122)-239, Department of Meteorology, University of California, Los Angeles (1952).

18. Z. Sekera, "Recent Developments in the Study of the Polarization of Skylight," Advances in Geophysics, III, pp. 43-104 (1956).

19. H. H. Kimball, "Measurements of Solar Radiation Intensity and Determinations of its Depletion by the Atmosphere," Monthly Weather Rev. 58, pp. 43-52 (1930).

20. J. N. Howard, D. L. Burch, and D. Williams, "Near-Infrared Transmission through Synthetic Atmospheres," Geophysics Research Papers, No. 40, AFCRC, Bedford, Mass. (1955).

21. J. E. McDonald, "Direct Absorption of Solar Radiation by Atmospheric Water Vapor," J. of Meteor. 17, 3, pp. 319-328 (1960).

22. D. Deirmendjian, "Atmospheric Scattering of Light and the Sun's Aureole," Scientific Report 1, Contract AF 19(604)-1303, Department of Meteorology, University of California, Los Angeles (1956).

23. K. L. Coulson, J. V. Dave, and Z. Sekera, Tables Related to Radiation Emerging from a Planetary Atmosphere with Rayleigh Scattering (University of California Press, Berkeley, Calif., 1960).

24. R. S. Fraser, Jr., "Scattering Properties of Atmospheric Aerosols," Scientific Report 2, Contract AF 19(604)-2429, Department of Meteorology, University of California, Los Angeles (1959).

25. H. C. Van de Hulst, "Scattering in the Atmospheres of the Earth and the Planets," Chap. III of Kuiper, G. P., The Atmospheres of the Earth and the Planets (University of Chicago Press, Chicago, Ill., 1947).

26. E. V. Piaskovskaia-Fesenkóva, "Some Properties of Atmospheric Light Scattering Function," Doklady Akad. Nauk, SSSR 88, 1, p. 53 (1953).

27. M. G. Gibbons, "Radiation Received by an Uncollimated Receiver from a 4π Source," J. Opt. Soc. Am., 48, 8, pp. 550-555 (1958).

28. L. A. Jones and H. R. Condit, "Sunlight and Skylight as Determinants of Photographic Exposure," J. Opt. Soc. Am. 38, 2, pp. 123-178 (1948).

29. H. G. Houghton, "On the Annual Heat Balance of the Northern Hemisphere," J. of Meteor. 11, 1, pp. 1-9 (1954).

30. M. J. Blackwell, R. H. Eldridge, and G. D. Robinson, Meteorological Research Paper 894, Air Ministry, London (1954).

31. P. A. Sheppard, "The Effect of Pollution on Radiation in the Atmosphere," Int. J. of Air Pollution 1, pp. 31-43 (1958).

32. R. A. Craig, "The Observations and Photochemistry of Atmospheric Ozone and Their Meteorological Significance," Meteor. Monograph Am. Meteor. Soc. 1, 2, (1950).

33. E. Vigroux, "Contribution a l'étude expérimentale de l'absorption de l'ozone," Doctoral Thesis, Université de Paris, Ser. A, No. 2542 (1953).

34. H. U. Dütsch, "Vertical Ozone Distribution over Arosa," Final Report, Contract AF 61(514)-905, Lichtklimatisches Observatorium, Arosa, Switzerland (1959).

35. K. R. Ramanathan and R. N. Kulkarni, "Mean Meridional Distributions of Ozone in Different Seasons Calculated from Umkehr Observations and Probable Vertical Transport Mechanisms," Quart. J. Roy. Meteor. Soc. 86, 368, pp. 144-155 (1960).

36. K. R. Ramanathan and J. V. Dave, "The Calculation of the Vertical Distribution of Ozone by the Götz Umkehr-Effect (Method B)," Annals of the I.G.Y., 5, pp. 23-45 (1957).

37. F. S. Johnson, "High-Altitude Diurnal Temperature Changes due to Ozone Absorption," Bull. Am. Meteor. Soc. 34, 3, pp. 106-110 (1953).

38. R. J. Murgatroyd and R. M. Goody, "Sources and Sinks of Radiative Energy from 30 to 90 km," Quart. J. Roy. Meteor. Soc. 84, 361, pp. 225-234 (1958).

39. J. Pressman, "Seasonal and Latitudinal Temperature Changes in the Ozonosphere," J. of Meteor. 12, 1, pp. 87-89 (1955).

40. R. A. Craig, "Radiative Temperature Changes in the Ozone Layer," Compendium of Meteorology, pp. 292-302 (American Meteorological Society, Boston, Mass., 1951).

STANFORD
RESEARCH
INSTITUTE

MENLO PARK, CALIFORNIA

REGIONAL OFFICES AND LABORATORIES

SOUTHERN CALIFORNIA LABORATORIES
820 Mission Street
South Pasadena, California

NEW YORK OFFICE
270 Park Avenue
New York 17, N. Y.

WASHINGTON OFFICE
711 14th Street, N. W.
Washington 5, D. C.

EUROPEAN OFFICE
Pelikanstrasse 37
Zurich 1, Switzerland

RESEARCH REPRESENTATIVES

HONOLULU, HAWAII
Finance Factors Building
195 South King Street
Honolulu, Hawaii

PORTLAND, OREGON
Suite 914, Equitable Building
421 Southwest 6th Avenue
Portland, Oregon

PHOENIX, ARIZONA
Suite 216, Central Plaza
3424 North Central Avenue
Phoenix, Arizona

UNCLASSIFIED

UNCLASSIFIED